Systematic determination of dust properties for a sample of 133 spatially resolved debris discs

J. P. Marshall [1]*, S. Hengst [2], R. Young,[3] F. Kemper [4,5,6] L. Matrà,[7] N. Pawellek [8,9]
H. Kobayashi,[10] P. Scicluna[11] and S. T. Zeegers[12]

[1]*Academia Sinica Institute of Astronomy and Astrophysics, 11F of AS/NTU Astronomy-Mathematics Building, No.1, Section 4, Roosevelt Rd, Taipei 106319, Taiwan*
[2]*Centre for Astrophysics, University of Southern Queensland, Toowoomba QLD 4350, Australia*
[3]*School of Physics and Astronomy, Vanderbilt University, 2301 Vanderbilt Place, Nashville, TN 3723, USA*
[4]*Institut de Ciències de l'Espai (ICE, CSIC), Can Magrans, s/n, E-08193 Cerdanyola del Vallès, Barcelona, Spain*
[5]*ICREA, Pg. Lluís Companys 23, E-08010 Barcelona, Spain*
[6]*Institut d'Estudis Espacials de Catalunya (IEEC), E- 08860 Castelldefels, Barcelona, Spain*
[7]*School of Physics, Trinity College Dublin, the University of Dublin, College Green, Dublin 2, D02 PN40, Ireland*
[8]*Institut für Astrophysik, Universität Wien, Türkenschanzstraße 17, 1180 Vienna, Austria*
[9]*Konkoly Observatory, Research Centre for Astronomy and Earth Sciences, Eötvös Loránd Research Network (ELKH), Konkoly-Thege Miklós út 15-17, 1121 Budapest, Hungary*
[10]*Department of Physics, Nagoya University, Nagoya, Aichi 464-8602, Japan*
[11]*Centre for Astrophysics Research, University of Hertfordshire, Hatfield, AL10 9AB, UK*
[12]*European Space Agency / ESTEC Keplerlaan 1, NL-2201 AZ, Noordwijk, the Netherlands*

ABSTRACT

Determination of the composition and size distribution of dust grains in debris discs is strongly dependent on constraining the underlying spatial distribution of that dust through multiwavelength, spatially resolved imaging spanning near-infrared to millimetre wavelengths. To date, spatially resolved imaging exists for well over a hundred debris disc systems. Simple analytical radiative transfer models of debris dust emission can reveal trends in disc properties as a function of their host stars' luminosities. Here, we present such an analysis for 133 debris discs, calculating the dust grain minimum sizes (s_{min}), dust masses (M_{dust}), and exponents of the size distribution (q) in conjunction with their architectures determined at far-infrared or millimetre wavelengths. The distribution of q at far-infrared to millimetre wavelengths is characterized, finding a value of $3.49^{+0.38}_{-0.33}$. We further newly identify a trend between q and R_{disc}, which may be indicative of velocity dependent fragmentation, or grain growth at large radii. We find the disc masses inferred from this analysis are consistent with those of protoplanetary discs. Finally, we identify samples of debris discs suitable for further characterization at millimetre and centimetre wavelengths, expanding the number of spatially resolved systems upon which future studies of these statistics can be based.

Key words: (stars:) circumstellar matter – infrared: planetary systems – radio continuum: planetary systems.

1 INTRODUCTION

Planetesimals, i.e. asteroids and comets, form within gas- and dust-rich protoplanetary discs. These minor bodies are the building blocks of planets. Not all planetesimals are swept up into planets during their formation, and remnant belts of planetesimals may persist for the lifetime of the host star and even beyond (see e.g. for recent reviews: J. Farihi 2016; A. M. Hughes, G. Duchêne & B. C. Matthews 2018). Once a high enough threshold velocity is reached, collisions between planetesimals within these belts produces a self-sustaining cascade of smaller bodies down to (sub-)micron-sized dust grains. This dusty debris most commonly reveals itself by the presence of excess emission above the stellar photosphere at infrared to millimetre wavelengths. Debris discs may therefore be considered larger, more massive analogues of the Solar system's Asteroid or Edgeworth–Kuiper belts (J. Horner et al. 2020).

To date, over 1 000 debris discs have been identified (P.-C. Cao et al. 2023), but the vast majority of these systems remain spatially unresolved. Knowledge of the underlying dust properties (e.g. grain-size distribution, composition, mass, etc.) is degenerated with radial extent (and width) of these discs (e.g. J. P. Marshall et al. 2014). Modelling of debris discs imaged at multiple wavelengths weakens that inherent degeneracy (e.g. R. J. Sylvester, M. J. Barlow & C. J. Skinner 1994; S. Ertel et al. 2011; S. Hengst et al. 2017, 2020). Dust emission at far-infrared and (sub-)millimetre wavelengths is sensitive to large dust grains that are unperturbed by radiation forces (A. V. Krivov 2010). These grains therefore trace the location(s) of the dust-producing planetesimal belt(s) within a system (N. Pawellek et al. 2019).

The minimum size of dust grains, s_{min}, in the dust-size distribution and their relation to the stellar parameters for a sample of spatially resolved debris discs from *Herschel* observations were investigated in N. Pawellek et al. (2014) and N. Pawellek & A. V. Krivov (2015). They found s_{min} consistent with being at, or a few times larger, than the blowout grain size s_{blow} (the size for which dust grains will be ejected from a system by stellar radiation pressure, see e.g. A. V. Krivov 2010), for all stars in the sample, consistent with collisional evolution of these discs. They further found no strong dependence of the relation between on s_{min} versus s_{blow} with grain composition or porosity. The absence of discs around lower luminosity stars with s_{min} close to s_{blow} was attributed to greater dynamical stirring in the discs of more luminous stars.

The size distribution of dust grains within a debris disc is often modelled as a continuous power law extending between minimum and maximum grain sizes with a differential form $dn \propto s^{-q} ds$. The size distribution exponent, q has been determined observationally either by fitting the slope of the sub-millimetre emission, or full radiative transfer modelling of the disc spectral energy distribution (SED). At mid-infrared wavelengths *Spitzer* detections of debris discs with a 10 μm silicate feature (T. Mittal et al. 2015) revealed a broad range of q values spanning 3.5–5 and peaking at 4. millimetre wavelengths a small sample of 22 discs reveals a much flatter $q = 3.31 \pm 0.07$ (M. A. MacGregor et al. 2016; J. P. Marshall et al. 2017; B. J. Norfolk et al. 2021). The value of q is oft assumed to be 3.5, consistent with a steady-state collisional cascade (J. S. Dohnanyi 1969; H. Tanaka, S. Inaba & K. Nakazawa 1996). Numerical models of dust distributions in collisional equilibrium converge on a slightly steeper value of $q = 3.65$ (A. Gáspár et al. 2012). Refinements to the Dohnanyi model including a size-dependent tensile strength of the colliding bodies and velocity-dependent fragmentation extend the potential range of q from 3 to 4 (e.g. D. P. O'Brien & R. Greenberg 2003; H. Kobayashi & H. Tanaka 2010). Collisional debris from more weakly bound 'rubble pile' bodies produces lower values of q (M. Pan & R. Sari 2005; M. Pan & H. E. Schlichting 2012), whereas fragmentation of monolithic bodies produces higher q values (W. Benz & E. Asphaug 1999; M. Pan & H. E. Schlichting 2012). The dust-size distribution deviates from a single power law due to the existence of a finite cut-off grain size at s_{min} introducing a 'wavy' pattern (A. V. Krivov, T. Löhne & M. Sremčević 2006; P. Thébault & J. C. Augereau 2007; P. Thebault & Q. Kral 2019). Inclusion of dust removal processes (e.g. Poynting-Robertson drag, stellar winds) can further alter the size distribution for the restricted range of grain sizes where those mechanisms are dominant (M. C. Wyatt, C. J. Clarke & M. Booth 2011). These waves are small in amplitude and have yet to be detected observationally. Degeneracies exist in the determination of q from radiative transfer modelling, most importantly with the assumed dust composition (T. Löhne 2020), which for most debris discs is unconstrained through the absence of solid state mid-infrared spectral features (e.g. C. H. Chen et al. 2014).

The dust mass of a debris disc can be inferred from millimetre wavelength emission, assuming the disc to be completely optically thin, and adopting a dust mass opacity (e.g. W. S. Holland et al. 2017). The inferred dust mass for debris discs is seen to evolve over time from high masses at younger ages to lower masses at later ages, consistent with the collisional evolution of a parent planetesimal population grinding down into dust (T. Löhne, A. V. Krivov & J. Rodmann 2008; J. R. Najita, S. J. Kenyon & B. C. Bromley 2022). Extrapolation of dust masses to total (planetesimal) masses for many of the brightest known debris discs are often in excess of what would be considered plausible for their initial protoplanetary disc masses (A. V. Krivov & M. C. Wyatt 2021).

In this work, we present an analysis for 133 systems out of an initial sample of 140 spatially resolved debris discs identified in surveys by *Herschel* (J. P. Marshall et al. 2021; A. M. Heras et al. 2025), the Sub-Millimeter Array and the Atacama Large Millimeter/sub-millimeter Array (A. Steele et al. 2016; L. Matrà et al. 2025). A large degree of overlap exists between the samples studied by these facilities such that many, but not all, spatially resolved discs have been observed by both. These surveys have revealed a rich variety of non-axisymmetric structures such as star-disc offsets, warps, and blobs. However, we do not concern ourselves here with accounting for the specifics of every disc architecture in this work. Our goal is to provide a uniform analysis of a large sample of spatially resolved discs to determine the properties of debris dust as a population rather than precise modelling of every individual system.

The remainder of the paper is laid out as follows. We present a summary of the underlying observations and the methods used to model the compiled data sets in Section 2. The modelling and analysis are presented in Section 3. A summary of the dust properties and their trends are given in Section 4. We compare our findings to previous studies of the dust grain properties of debris discs in Section 5 before presenting our conclusions in Section 6.

2 OBSERVATIONS

The sample of discs underlying this study was assembled from literature studies of debris discs that have been spatially resolved in thermal emission. We focus on the analyses of spatially resolved discs with *Herschel* published in J. P. Marshall et al. (2021) and A. M. Heras et al. (2025), representing the largest such homogeneous sample, and at millimetre wavelengths the REASONS (ALMA and SMA) sample of L. Matrà et al. (2025) along with additional systems from A. Steele et al. (2016). For these studies the disc architectures were modelled in a consistent fashion facilitating their combination and comparison. We do not include discs that have only been resolved in scattered light (e.g. T. M. Esposito et al. 2020), or young debris discs in star forming regions (e.g. J. Lieman-Sifry et al. 2016) that lack sufficient photometry at infrared wavelengths to model the dust emission. There were 140 individual systems within the combined data set that formed our initial sample, with 74 systems with architectures coming from ALMA or SMA observations and 66 systems with resolved extents based on *Herschel* observations.

The photometric data and stellar atmosphere models assembled for each system were taken from the stellar data base (SDB),[1] for which the methods are presented in B. Yelverton et al. (2019). The photometry used in determination of the infrared excess predominantly come from observations by *WISE* (E. L. Wright et al. 2010), *Akari* (D. Ishihara et al. 2010), *Spitzer* (K. Y. L. Su et al. 2006; G. Bryden et al. 2009; C. H. Chen et al. 2014), *Herschel* (C. Eiroa et al. 2013; N. D. Thureau et al. 2014; B. Montesinos et al. 2016; G. M. Kennedy et al. 2018), JCMT/SCUBA-2 (W. S. Holland et al. 2017), the SMA and ALMA (A. Steele et al. 2016; L. Matrà et al. 2025).

A warmer, inner component was identified around 33 debris disc systems in the sample.[2] These were identified using SED fitting of modified blackbodies to the excess emission and MULTINEST to discriminate between one and two component models for the debris discs (B. Yelverton et al. 2019). The contribution of a warm component to the total emission of a system was subtracted from the measured fluxes prior to radiative transfer modelling so as not to

---

[1] http://drgmk.com/sdb/

[2] These systems are identified in Table A1.

bias the results of our analysis. We complement the data taken from the SDB with additional photometry, predominantly at millimetre wavelengths, which were absent from the compiled data sets within the repository (e.g. HD 16743, HD 138965; J. P. Marshall et al. 2023, 2025).

3 MODELLING AND ANALYSIS

Modelling the dust emission of the debris disc sample was undertaken using the Python-based 1D analytical radiative transfer code ARTEFACT[3] (J. P. Marshall et al. 2023). As inputs to the code we took the radius and width of the disc from the imaging observations, and the compiled photometry, stellar parameters, and photosphere model from SDB.

For the disc architectures, each system was modelled as a Gaussian ring, with an architecture defined by a flux density f_{disc}, peak radius R_{disc}, fractional width ΔR_{disc}, inclination i, and position angle ϕ. When assigning an architecture for each system, we preferentially selected the architecture derived from ALMA as having the best combination of angular resolution and signal-to-noise ratio, followed by the SMA, and lastly *Herschel*. The sole exception to this procedure was HD 48682, for which the SMA detection is marginal and the *Herschel* data are therefore a better constraint on the disc architecture (S. Hengst et al. 2020).

For the dust composition we used the complex optical constants n and k of astronomical silicate (B. T. Draine 2003), with dust optical properties calculated by Mie theory using the PYTHON package MIEPYTHON[4] (S. Prahl 2024). The total sample of discs was split into two parts on the basis of the availability of (sub-)millimetre photometry beyond 450 μm to constrain the particle-size distribution. For those systems with sufficient data, we fitted the minimum grain size s_{min} (with a fixed $s_{max} = 3$ mm), exponent of the size distribution q, and dust mass M_{dust}. For systems without sufficient data at (sub-)millimetre wavelengths to constrain the size distribution exponent q was held fixed as 3.5 in the modelling. We model the SEDs of all systems out to 10 mm for comparison with existing long-wavelength measurements (M. A. MacGregor et al. 2016; B. J. Norfolk et al. 2021).

The parameter space was explored using EMCEE (D. Foreman-Mackey et al. 2013). For each system we initialize 50 walkers with randomly generated, uniformly distributed values of $\log_{10} s_{min}$ between -1 and 1 (in μm), $\log_{10} M_{dust}$ between -6 and -3 (in $M_{\oplus}$), and q between 3.8 and 3.2. The bounds on the parameters were $\log_{10} s_{min}$ between -2 and 2, $\log_{10} M_{dust}$ between -9 and 0, and q between 2 and 5. For each realization of the model a least-squares fit was made to the observations and passed to EMCEE as the log probability. We ran the walkers in chains with a burn-in of 100 steps and thereafter until all parameters had passed a threshold of 50 autocorrelation times, which was typically achieved in around 2 000 steps. The posterior probability distribution was assembled using the final 10 000 realizations of the model. The posterior probability distributions were generally monomodal and normally distributed, although several systems had a pronounced skew to either s_{min} or q; these findings will be detailed in the following sections. The final maximum amplitude probability model parameters for each disc (s_{min}, M_{dust}, and q where possible) and their associated uncertainties were determined using the 16th, 50th, and 84th percentiles of the distribution.

4 RESULTS

Here we present the statistics and trends for the three dust properties, i.e. minimum grain size, exponent of the size distribution, and dust mass, considered in this analysis. These were compared against system properties, such as the stellar luminosity and disc radius, to search for trends in their behaviour. Some of these trends have been previously identified, such as the relationship between minimum grain size and stellar luminosity (N. Pawellek et al. 2014), but the expanded sample size presented here makes revisiting these trends worthwhile. A complete summary of the results of the radiative transfer modelling are provided in tabulated form in Appendix A.

4.1 Anomalous SEDs

The first result we must note is that seven of the 140 systems modelled in this work have SEDs that do not adequately match the observations. Six of the systems, HD 25821, HD 32977, HD 36546, HD 113766, HD 158643, and HD 278932, are distinct from the bulk of the modelled systems through the very small minimum grain size (≤ 0.2 μm) derived in the modelling. These systems have poorly sampled SEDs with only one or two far-infrared data points constraining the cold excess and evidence of substantial mid-infrared excess in *WISE* W3 and/or W4 bands. The far-infrared emission for those sources being poorly constrained means that modelling cannot meaningfully constrain the dust properties of the debris disc. Exhibiting substantial mid-infrared excess suggests these systems could be younger, less-evolved discs. The radiative transfer code used for this analysis is unsuitable to model such systems and they have therefore been omitted from further analysis.

The final system, HD 90089, has a relatively cold excess (peaking at 160 μm), similar to the 'cold debris discs' identified by Herschel DUNES (C. Eiroa et al. 2011; A. V. Krivov et al. 2013; J. P. Marshall et al. 2013). Radiative transfer modelling reveals the spatially resolved extent of HD 90089's disc is inconsistent with the low temperature of the excess emission, from which we may infer the excess may instead be due to contamination from a background galaxy. Omitting all of these unusual systems from the total sample leaves a population of 133 debris discs which we examine in the remainder of this section.

4.2 Minimum grain size

The relationship between the calculated minimum grain size, s_{min}, and the blowout grain size, s_{blow}, for each system (a function of stellar luminosity) is shown in Fig. 1. A clear trend of increasing minimum grain size as a function of stellar luminosity is seen in the sample. We model the sample distribution with a power law following N. Pawellek et al. (2014) using an error-weighted least-squares fit obtaining a slope and intercept of 0.21 and 2.1 μm, respectively. This is consistent with the previous determination based on the smaller sample used by N. Pawellek et al. (2014), who found slope and intercept values of 0.20 ± 0.07 and 3.2 ± 0.7, and statistically significant with a Spearman correlation coefficient of 0.29 and a p-value of 0.007. Below 1.05 $L_{\odot}$ we can calculate that the stellar radiation pressure will not be sufficient to remove dust grains from the system (J. A. Burns, P. L. Lamy & S. Soter 1979), therefore the blowout grain sizes for those low luminosity are not meaningful. The equivalent blowout grain size for 1.05 $L_{\odot}$ is 0.37 μm and is denoted by the hatched region in Fig. 1. At intermediate stellar luminosities, a mixture of systems with minimum dust grain sizes both above and below the blowout radius is present in the sample. Above 20 $L_{\odot}$ all of
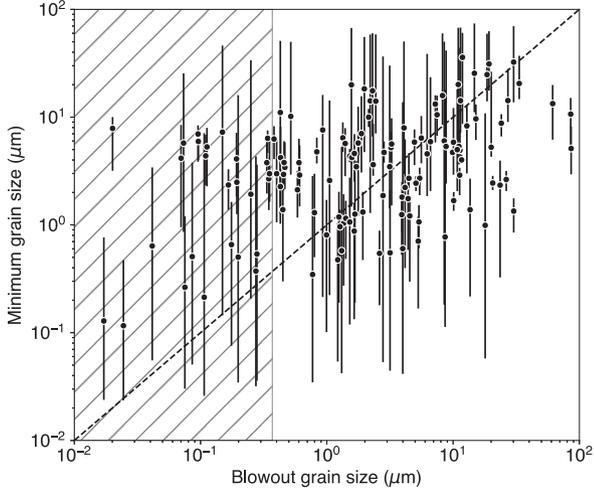
Figure 1. Plot of s_{min} versus s_{blow}. The dashed line denotes equivalence between s_{min} and s_{blow}, while the hatched region denotes the range of calculated blowout grain sizes that are not meaningful as the associated stellar luminosity is too small to produce high β grains. It is clear that for most systems, particularly around high luminosity stars, a substantial contribution to their excess emission comes from sub-blow out grains.

the debris discs have a minimum grain size smaller than the blowout radius, such that the dust emission observed at infrared wavelengths comes predominantly from transient dust grains (P. Thebault & Q. Kral 2019).

For a minority of systems the upper bound of the dust grain size is poorly constrained (i.e. the positive error bar on s_{min} is large). This is a natural consequence of modelling sparsely sampled SEDs. The systems for which this is true are predominantly those for which we have weak, or non-existent constraints on the sub-millimetre slope, particularly bridging the gap between far-infrared and millimetre photometry. Improving these results will require a dedicated campaign of observation to fill in the required observations.

In Fig. 2, we present the ratio of s_{min}/s_{blow} as a function of stellar luminosity and the exponent of the size distribution. In both panels, shaded regions denote the regions of stellar luminosity below which there is no blowout radius for astronomical silicate dust grains ($L_\star \leq 1.05\,L_\odot$) and below which there is a range of dust grains removed by radiation pressure ($1.05\,L_\odot < L_\star \leq 6.15\,L_\odot$). Above $6.15\,L_\odot$ there is a singular minimum bound grain size for each system. Uncertainties on s_{min} are largest for discs with weak constraints on their sub-millimetre emission, lacking photometric data between 160 and 850 μm. There is a clear trend between the stellar luminosity and the ratio s_{min}/s_{blow}, albeit with substantial scatter and large intrinsic uncertainties in the determination of s_{min}. A linear regression fit using the SCIPY function *linregress* finds a Spearman correlation coefficient of -0.69 and a p-value 10^{-16}, demonstrating the sample has a distribution strongly deviating from a flat slope. Comparison between the modelling presented here and previous results from N. Pawellek et al. (2014) and N. Pawellek & A. V. Krivov (2015) studying a smaller sample of 32 discs (all of which are included in this analysis). The dependence of s_{min}/s_{blow} is much steeper here than the trend for astronomical silicate dust presented in N. Pawellek & A. V. Krivov (2015) (shown in Fig. 2). Their sample was smaller, lacked the high-resolution architectures at millimetre wavelengths, and had no constraints on the disc widths. The higher angular resolution data result in larger inferred disc radii for the systems in this sample, such
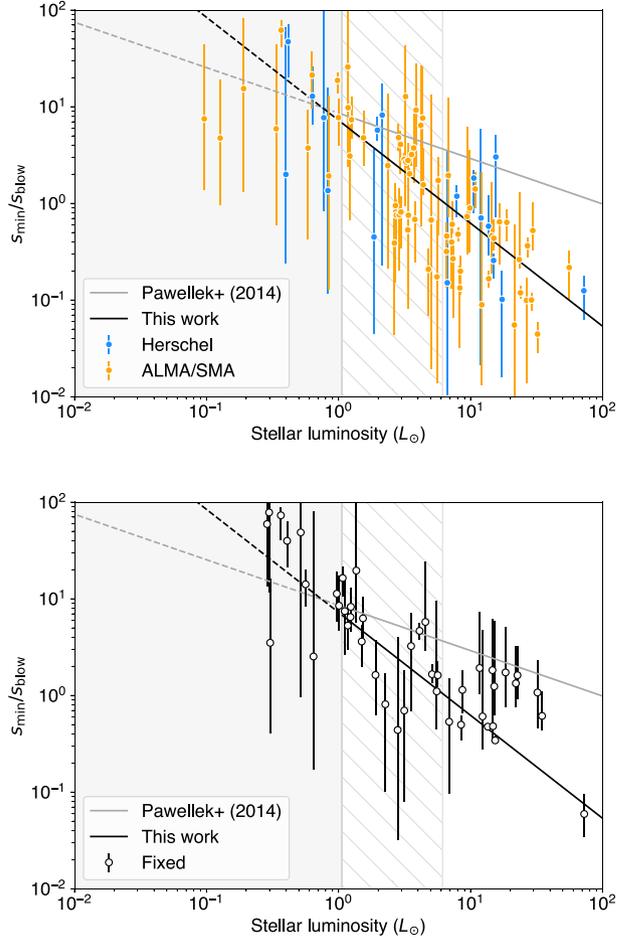

Figure 2. *Top*: Plot of s_{min}/s_{blow} versus $L_\star$. Blue data points are for *Herschel*-resolved architectures, whereas orange data points are for ALMA- or SMA-resolved architectures. Uncertainties are 1σ. The shaded region denotes stellar luminosities for which no blowout grain size exists and the hatched region denotes stellar luminosities for which a range of grain sizes are blown out. The two straight lines denote the relationship between s_{min}/s_{blow} determined by N. Pawellek et al. (2014) (grey line) and the fit to the ensemble presented here (black line). *Bottom*: Same as above, except the white data points denote discs with $q = 3.5$.

that s_{min} is decreased and the overall slope of the distribution becomes steeper.

4.3 Exponent of the dust-size distribution

Out of the 133 systems, 96 have sufficient photometric coverage at (sub-)millimetre wavelengths to make a determination of the dust grain-size distribution exponent q from SED modelling. Debris discs typically have values of q between 3 and 4. All of the systems modelled here have measured exponents within the range 2–5 with 89 systems having measured values between 3 and 4. Typical uncertainty in the measurement of q is ± 0.25 for the sample. Outliers with much larger uncertainties in q (up to ± 1.0) are present in the results, and those systems are characterized by having only photometry shortward of 450 μm constraining their sub-millimetre slopes – sufficient to model q as a free parameter, but only enough to weakly constrain it.

The discs with the steepest exponents are HD 113556, HD 158633, and HD 159492, for all of which $q > 4$. The sharp drop off in their submillimetre SEDs are reminiscent of the 'steep SED' discs
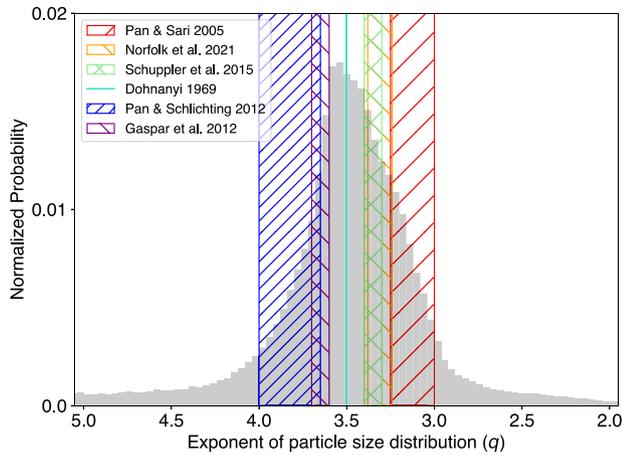
Figure 3. Histogram of q values derived from modelling. The distribution is assembled from the posterior probability distributions of individual systems. Hatched regions on the plot denote the regions associated with q expected for different collisional models (see the text for details).

identified at far-infrared wavelengths by S. Ertel et al. (2012). However, the large uncertainties leave the range of possible q values consistent with typical debris discs for all three systems, leaving their true nature ambiguous. At the flatter end of q values, HD 27290, HD 48370, HD 109085, and HD 131488 all have $q < 3$. Again, the associated uncertainties mean the calculated values for these systems are not significantly above the expected range for q. All four systems exhibit observational properties consistent with a large contribution from small (warm) dust grains exhibiting strong mid-infrared excesses (H. Broekhoven-Fiene et al. 2013; A. Moór et al. 2016; N. Pawellek et al. 2024), and HD 109085 in particular having dust spectral features associated with a giant collision event (C. M. Lisse et al. 2012).

The overall distribution of q is presented in Fig. 3, and is derived from the posterior probability distributions of the individual fits. Based on the probability distribution the median value of q is $3.49^{+0.38}_{-0.33}$, consistent with the infinite steady-state collisional cascade of J. S. Dohnanyi (1969) and H. Tanaka et al. (1996). The distribution can be seen to have a slight skew towards flatter rather than steeper values (compared to a value of 3.5), but it is not significantly skewed. We compare the measured values of q in Fig. 3 to various theoretical (M. Pan & R. Sari 2005; M. Pan & H. E. Schlichting 2012; A. Gáspár, G. H. Rieke & Z. Balog 2013) and observational results (C. Schüppler et al. 2015; B. J. Norfolk et al. 2021). The theoretical modelling can reproduce values of q in the range 3 to 4, depending on the assumptions. D. P. O'Brien & R. Greenberg (2003) demonstrated analytically that a range of q beyond the 3.5 obtained under the assumptions of J. S. Dohnanyi (1969) can be obtained by consideration of the tensile strength of the colliding bodies, with weakly bound bodies ('gravity regime') having $q < 3.5$ and strongly bound bodies ('strength regime') having $q > 3.5$. In the presence of a size-dependent velocity distribution and viscous damping of the collision fragments further modifications to q are obtained in the gravity regime ($q \simeq 3$ M. Pan & R. Sari 2005; M. Pan & H. E. Schlichting 2012), and strength regime ($q > 3.65$ M. Pan & H. E. Schlichting 2012). The expected range of q is further dependent on the relative velocities of the bodies involved in the collision. In A. Gáspár et al. (2012), good consistency for a broad range of disc models in collisional equilibrium is found, converging to a value of $q = 3.65 \pm 0.05$, with some small dependence on the disc width and scale height. For comparison between populations we calculate the
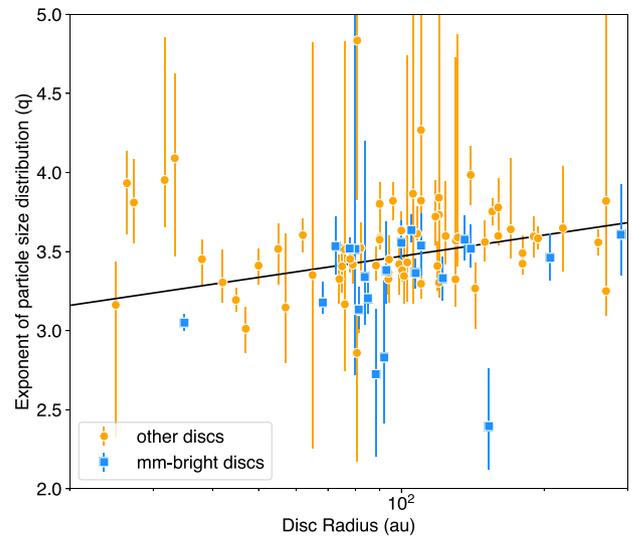

Figure 4. Plot of q versus R_{disc}. Circular data points are for systems for which q could be determined from modelling. Square data points denote systems that have also been detected at 7 or 9 mm (dubbed 'mm-bright'). The solid line denotes a power law fit to the observations illustrating a trend between R_{disc} and q.

error-weighted mean of the sample, being $q = 3.45 \pm 0.08$, which is slightly higher but still consistent with the value derived from millimetre-wavelength measurements of $q = 3.31 \pm 0.07$ from B. J. Norfolk et al. (2021), and lower than the distribution of q for mid-infrared discs observed by *Spitzer*, which peaked around 4.0 (T. Mittal et al. 2015). This suggests an evolution in the measured value of q as a function of wavelength (contributing grain size), with the far-infrared to millimetre derived slopes being broadly consistent. We note that the value of q at mid-infrared wavelengths is determined from discs with solid-state silicate features such that it is unclear if the inferred value of q is representative of either the small grains producing the spectral features or the bulk of the dust.

Previously there has been some suggestion that the presence of cold molecular CO gas in a debris disc may moderate collisions between dust grains and thereby influence the size distribution (B. J. Norfolk et al. 2021). A population of around 20 systems with gas have been identified to date encompassing both molecular gas and atomic line detections (S. Marino et al. 2020). In this sample there are 11 debris discs with CO gas detections, which are predominantly around young, early-type stars (A. Moór et al. 2017). The abundance of gas in these systems is such that its origin may be either primordial or generated in planetesimal collisions (Q. Kral et al. 2017; S. Marino et al. 2020). We can compare the calculated values of q for the systems with detected gas in the sample versus the overall distribution to see if they are statistically different. Within the same range of stellar luminosities (6.6–24 $L_\star$) there are another 30 stars in the sample. Examining the distribution of both s_{min} and q for gas-bearing systems as a function of $L_\star$, we find that both are consistent with the distribution of the wider sample.

We find a trend between q and R_{disc} as shown in Fig. 4. We fit the distribution of q vs R_{disc} with a straight line ($q = m \log_{10}(R_{\mathrm{disc}}) + c$) using the SCIPY *lmfit* routine finding best-fitting parameters of $m = 0.49 \pm 0.09$ and $c = 2.48 \pm 0.18$. The significance of this trend can be characterized by the Spearman correlation coefficient (ρ_s). The statistic $\rho_s = 0.26$ and probability $p = 0.013$ were calculated using the SCIPY *stats.spearmanr* function, suggesting a positive correlation exists between q and R_{disc} (or rather, it is highly unlikely
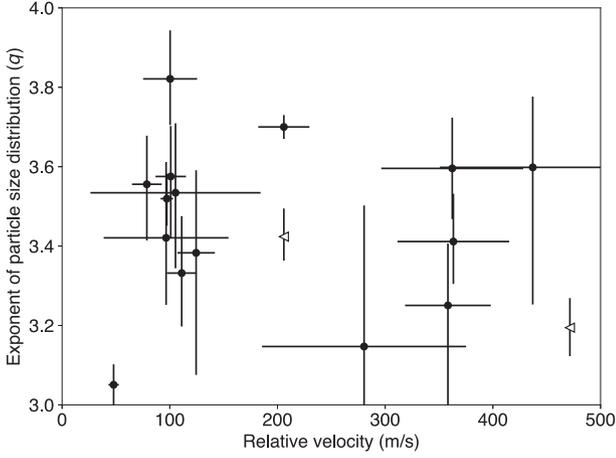
Figure 5. Plot of q versus v_{rel}. Data points are for debris discs with measured q values from this work and the relative velocities are calculated from the disc scale heights in J. Terrill et al. (2023). We see no strong trend between q and v_{rel}, contrary to what might expected from theoretical modelling (A. Gáspár et al. 2012), suggesting other factors are contributing to the value of q determined from the observations.

we would see the observed distribution if no correlation existed). We test the robustness of this correlation by fitting the trend to the systems with ALMA-derived radii finding values of $\rho_s = 0.35$ and $p = 0.005$, such that the significance of the correlation is increased; the majority of sources have ALMA data and these generally have lower uncertainties due to greater precision and denser sampling of the source SEDs.

The parameters of the best-fitting trend are consistent with $q \propto \sqrt{R_{disc}}$ or equivalently $q \propto 1/v_{Kep}$. Modelling by A. Gáspár et al. (2012) showed that the dust-size distribution becomes flatter for higher collisional velocities within debris discs (between 0.1 and 3 km s^{-1}), but the Keplerian velocity of a body is not representative of its collisional velocity. A handful of debris disc systems have had their vertical scale heights measured with values of h ranging between 0.02 and 0.21 (J. Terrill et al. 2023). Assuming the scale height is a proxy for dynamical stirring (i.e. systems with larger h have larger collision velocities), we should see in Fig. 5 that the value of q is anticorrelated with h. However, this is not the case due to the intrinsic scatter and the large uncertainties in both q and v_{rel}. Alternatively, the relationship could be interpreted as evidence for dust grain growth in the outskirts of larger debris discs where relative impact velocities are lower (T. Kadono, H. Kobayashi & M. Yokoyama 2024).

4.4 Dust mass and disc mass

We calculate dust masses for grains up to 3 mm for the debris discs in this work. In Fig. 6, we present the disc masses for the systems in this sample as a function of the mass of the host star. These masses are calculated using the equations from A. Krivov & M. C. Wyatt (2021), assuming power law size distributions of $q_{med} = 3.7$ between 3 mm and 1 km, and $q_{large} = 2.8$ between 1 and 200 km, the assumed radius of the largest bodies in the planetesimal belt. For the three systems with $q \geq 4$ the disc mass extrapolation from A. V. Krivov & M. C. Wyatt (2021) is inappropriate, so we instead adopt a mass opacity and calculate the dust masses for these systems from the measured (or interpolated) flux density at 1.3 mm and then integrate the three power laws across the same size ranges.
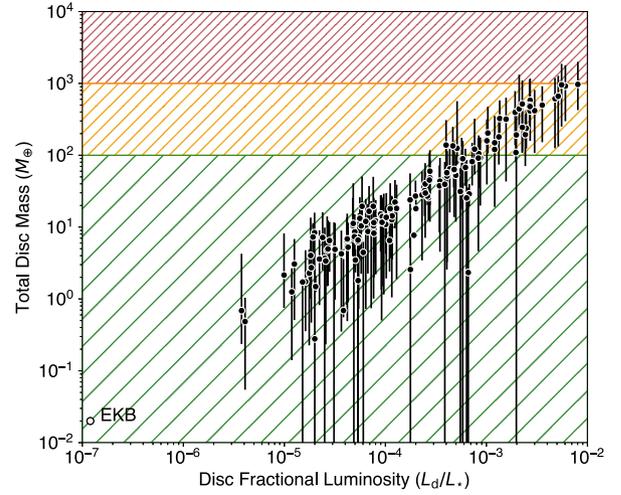

Figure 6. Plot of M_{disc} versus $L_d/L_\star$. Black data points denote masses calculated using a three component power-law size distribution for bodies up to 400 km in size following A. V. Krivov & M. C. Wyatt (2021) with the hatched regions denoting regions for which disc masses were considered marginal or too large based on the same analysis. The white labelled data point denotes the Edgeworth–Kuiper belt.
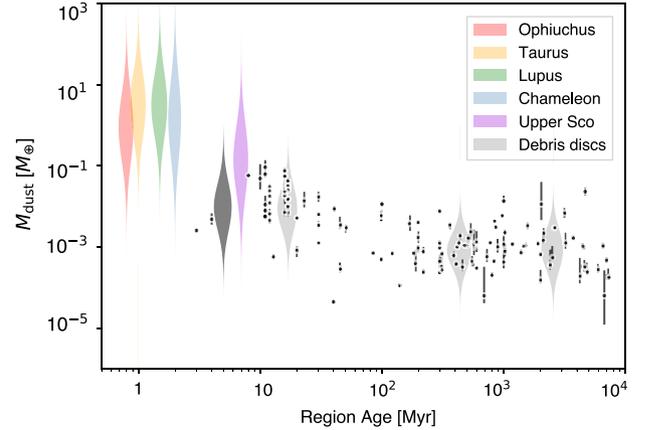

Figure 7. Violin plot of M_{dust} versus time comparing the dust masses for star forming regions against the distribution of debris discs. Coloured shaded regions show the distributions for the Chameleon, Lupus, Ophiucus, Taurus, and Upper Sco star-forming regions, following C. F. Manara et al. (2023) (see the text for details). The light grey shaded regions show the same distribution for debris disc dust masses for three age ranges, $t = 10$–100, 100–1000, and 1000–10 000 Myr, plotted at the median age for each interval. The dark grey shaded region shows the backward extrapolated dust mass of the ensemble for $t = 5$ Myr based on the disc evolution models of M. C. Wyatt et al. (2007). Solid data points show the calculated dust masses for the debris disc sample.

Contrary to the results of A. V. Krivov & M. C. Wyatt (2021), we find that none of the disc masses determined from this work are excluded based on the inferred masses of protoplanetary discs.

We also compare the distribution of dust masses for the ensemble to values determined for star forming regions. In Fig. 7, we present the distribution of dust masses for several nearby star forming regions, namely Chameleon (I. Pascucci et al. 2016; F. Long et al. 2018; M. Villenave et al. 2021), Lupus (M. Ansdell et al. 2016, 2018; L. I. Cleeves et al. 2016; T. Tsukagoshi et al. 2019; E. Sanchis et al. 2020), Ophiucus (J. P. Williams et al. 2019), and Taurus (S. M. Andrews et al. 2013; R. L. Akeson & E. L. N. Jensen 2014; K. Ward-Duong
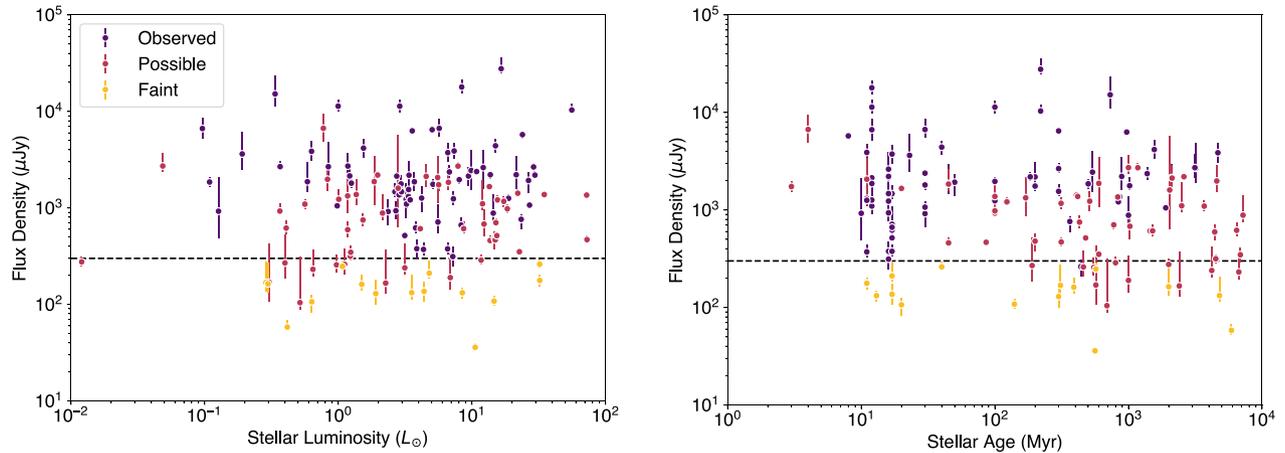
Figure 8. Here, we show the potential for additional spatially resolved millimetre wavelength imaging to add to the ensemble of debris discs. The distribution of predicted (and observed) disc flux densities are presented as a function of stellar luminosity (left) and system age (right). Coloured data points denote existing observations (purple), possible detections (red) and faint sources (orange). The dashed line at 300 μJy lies close to the limit of current detections. A total of 47 discs lie around or above this limit, representing a substantial potential addition to the REASONS sample of 74 systems (L. Matrà et al. 2025).

et al. 2018; R. L. Akeson et al. 2019; F. Long et al. 2019), and Upper Sco (J. M. Carpenter, L. Ricci & A. Isella 2014; S. A. Barenfeld et al. 2016; G. van der Plas et al. 2016), against the calculated dust masses from this work. The debris disc dust mass distribution at 5 Myr is calculated by backward extrapolation using the stellar ages and observed radii following the model of M. C. Wyatt et al. (2007). While this method is fraught with uncertainty, particularly for older stars (> 100 Myr) whose ages are only weakly constrained, we find that the inferred debris disc dust masses are broadly consistent with the distributions of class II discs in nearby star forming regions.

4.5 Comparison of predicted and observed millimetre fluxes

4.5.1 Band 6 predictions

In addition to the fitted dust parameters presented in the previous sections, we obtain predicted flux densities for the debris discs for those systems that have not yet been spatially resolved at (sub)millimetre wavelengths. We assumed the value of q to be 3.5 for those discs without millimetre photometry, which coincidentally lies close to the peak of the observed distribution (as shown in Fig. 3), such that these predictions should be relatively accurate. A summary of the Band 6 (1.3 mm) flux density predictions as a function of stellar luminosity and system age are presented in Fig. 8.

Amongst the 133 debris discs analysed in this work, 74 were part of the REASONS survey with high-quality millimetre photometry (L. Matrà et al. 2025). A further 20 had sub-millimetre photometry from another observatory (e.g. JCMT, W. S. Holland et al. 2017), but were not observed at high angular resolution, and the remaining 39 systems lack any constraints on their millimetre brightness or architecture.

We find that there exists an untapped population of far-infrared spatially resolved discs across the full range of stellar luminosities. These as-yet-unobserved systems are generally fainter ($F_{disc} \leq 1$ mJy) and found predominantly around older stars ($t_\star > 100$ Myr). As such they occupy an under explored region of parameter space for both disc and disc-planet interaction. Based on observation with the ALMA 12-m array, we can define a disc as observable if its diameter can be spatially resolved by ≥ 3 beams with a signal-to-noise ≥ 5 per beam, equivalent to the REASONS sample. For a face-on disc with a diameter of 3 beams and an unresolved belt width, this requires an

rms of 10 μJy per beam, and an integrated flux density of 300 μJy (equivalent to the horizontal dashed line in Fig. 8).

Not all as-yet-undetected debris discs are amenable to characterization by ALMA. Some lie too far north for observation (although the SMA or NOEMA could serve instead), are too extended on the sky, or their integrated flux densities are too low for high-angular resolution observations. Under these constraints, a further 47 systems are potentially characterizable, representing an $\simeq 50$ per cent addition to the ensemble of millimetre-wavelength spatially resolved debris discs. The measurement of these additional discs at millimetre wavelengths would in almost all cases provide a first unique measurement of q (and M_{dust}) for those systems and substantially reduce the uncertainties on s_{min} (particularly its upper bound, see Table A1). The improvement on the uncertainties of the calculated parameters for the ensemble would be $\simeq 20$ per cent.

4.5.2 Band 1 predictions

We further calculated the SEDs of the debris discs to $\lambda_{max} = 10$ mm in order to compare the predicted and observed emission for the small population of debris discs which have ATCA or VLA measurements at 7 or 9 mm (L. Ricci et al. 2012, 2015; M. A. MacGregor et al. 2016; J. P. Marshall et al. 2017; B. J. Norfolk et al. 2021). We find that for most detected systems the observed flux densities are a factor of two to three higher than the predicted emission from our radiative transfer modelling, a minority of the systems are consistent with our predictions, and none are significantly fainter. We plot the results of this comparison in Fig. 9. The estimates for $\simeq$ cm wavelength emission from debris discs derived from fitting infrared to (sub-)millimetre photometry are therefore conservative in their predictions.

Stellar chromospheric activity can produce enhanced emission at millimetre to centimetre wavelengths above the level expected for simple stellar photosphere models (S. R. Cranmer, D. J. Wilner & M. A. MacGregor 2013; R. Liseau et al. 2015; J. A. White et al. 2018). Chromospheric emission for A type stars agrees with model predictions but the degree of excess chromospheric emission increases towards later spectral types (A. Mohan et al. 2021). The greatest amount of chromospheric excess is $\simeq 80$ per cent of the predicted stellar photospheric model, such that this could not account
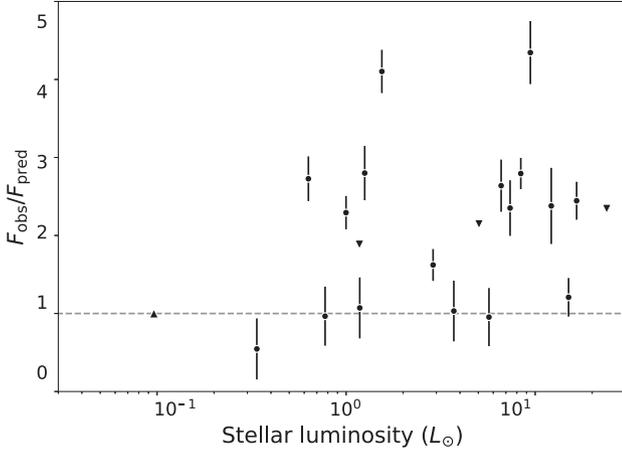
Figure 9. Plot of predicted and observed deep millimetre fluxes for systems in this work, separated by $L_\star$. The majority of detected discs have fluxes greater than the predictions made here indicating either a strong contribution from stellar chromospheric emission, or a flatter size distribution for the dust at millimetre to centimetre wavelengths. No system is observed to be significantly fainter than the predicted emission, such that determination of the detectability of a disc made from extrapolation should be considered reliable.

for the disparity between the radiative transfer model predictions and measured flux densities.

Recent modelling of discontinuous and power-law size distributions for dust grains in debris discs by M. Kim & S. Wolf (2024) provides an immediate explanation for the differences, as their work predicts overabundant small grains in a debris disc results in a flattening of the millimetre spectral slope compared to the sub-millimetre slope. Indeed, almost all systems for which we have enhanced long-wavelength emission (compared to our prediction) are known to have haloes of small dust grains.

In addition to the already existing population of 7- or 9-mm detected discs (B. J. Norfolk et al. 2021), the modelling presented here points to a further 20 discs that would be detectable with ALMA Band 1 without the need for elevated millimetre–centimetre emission (i.e. $F_{7mm} \geq 15\,\mu$Jy, consistent with existing detections at 3–5σ). However, these systems would not be spatially resolved such that the relative contribution from the stellar chromosphere could not be independently constrained for a 'clean' measurement of the millimetre–centimetre spectral index for these systems.

5 DISCUSSION

All debris discs are assumed to consist of dust grains with a composition of astronomical silicate (B. T. Draine 2003). This is primarily problematic on the basis that astronomical silicate is not a real material per se, despite its wide-found usage to fit dust emission. The secondary problem with this assumption is that there is good theoretical and observational evidence for water ice at the $\simeq 10$ per cent level in debris disc dust grains (e.g. A. Gáspár et al. 2012; F. Y. Morales et al. 2016; É. Choquet et al. 2018; J. P. Marshall et al. 2018), and the recent direct detection of ice around HD 181327 (C. Xie et al. 2025). The presence of icy inclusions in silicate dust grains has two effects on the inferred dust parameters from our models; it increases the minimum grain size s_{min} and flattens the exponent of the size distribution q (T. A. Stuber & S. Wolf 2022). However, not all debris discs need icy grains to fit their emission and the inferred fraction of ice required is also different for each system.

Similar effects on s_{min} and q are seen for enhanced porosity. Imaging polarimetry of debris discs suggest high porosity dust is required to match the observed polarizations at near-infrared wavelengths (T. M. Esposito et al. 2020), although this is not true of all systems (e.g. J. P. Marshall et al. 2020). Since the true composition (and structure) of debris dust is largely unknown, and whatever biases this assumption introduces should be systematic, we expect that it would not affect the overall conclusions of this work.

As a simplifying assumption for the radiative transfer modelling the dust grain properties in the disc are universal with the same size distribution and minimum/maximum grain sizes at all radii within a given disc. From the results we clearly see that for a broad range of stellar luminosities that the minimum grain size is below the radiation blowout limit for the star. A substantial contribution to the total dust emission therefore comes from dust grains close to that limit. Such grains would be impacted by radiation forces driving them on to higher eccentricity orbits outside their point of formation within the debris belt, whereas larger grains would not be (as strongly) affected. Redistributing smaller grains to larger radii around a star lowers their temperature, such that reproducing the observed emission of the disc would require a smaller minimum grain size and flatter size distribution for the dust grains.

For the observations being modelled here we adopted a largest grain size for the dust $\simeq$ the longest wavelength of observation (i.e. $s_{max} \simeq \lambda_{max}$). However, larger grains up to cm sizes contribute a small fraction of the total dust emission at those wavelengths. We are therefore systematically underestimating the total emission at the longest wavelengths in our models. However, this effect is relatively small to begin with, being around 5 per cent of the total emission at 1.3 mm, and comparable in magnitude to the uncertainty on the observations. The impact of the absence of cm-sized grains from the model will also be smaller for the steeper size distributions, such that their inclusion would not serve to substantially reduce the trend of q with R_{disc} identified in Fig. 4.

We identified a significant slope to a power law fit between disc radius R_{disc} and q within the sample of debris discs. The slope is consistent with dependence of q on $1/\sqrt{R_{disc}}$, which may be interpreted as $q \propto v_{Kep}$. The physical basis of this relationship is uncertain. We see no strong dependence between q and v_{rel} by way of inferring the scale heights for vertically resolved discs which might point to its origin as dust-size dependence on collision velocity (see Fig. 5).

6 CONCLUSIONS

We have modelled the spectral energy distributions for a sample of 133 spatially resolved debris disc systems. We calculated the minimum grain size, size distribution exponent, and dust masses for the sample. Based on the maximum likelihood models from the spectral energy distributions we further calculate predicted flux densities for these discs at 1.3 and 7 mm, analogous to ALMA bands 6 and 1, respectively.

Consistent with previous analyses of a smaller sample of 34 spatially resolved discs examined by N. Pawellek et al. (2014), we recover the same trend in $L_\star$ vs. s_{min}. With the larger sample examined here we find that the majority of discs around stars above 20 $L_\odot$ have values of s_{min} below the blowout limit, implying that a substantial population of grains small enough to be blown out by radiation pressure contributes to their observed far-infrared emission, consistent with the findings of P. Thebault & Q. Kral (2019).

We determine the median-size distribution exponent to be $q = 3.49^{+0.38}_{-0.33}$. The majority of debris discs have size distribution ex-

ponents q within the range 3–4, consistent with being dictated by the strength of the colliding bodies (M. Pan & H. E. Schlichting 2012). A handful of outlier systems are found both above and below this range, albeit with uncertainties large enough to render them formally consistent with the expected range of $4 > q > 3$ for debris dust. We further identify a trend between R_{disc} and q for these systems. Interpretation of this trend is uncertain, being attributable to either velocity dependent collisional fragmentation (A. Gáspár et al. 2012) or grain growth in the outer regions of debris discs (T. Kadono et al. 2024). Additional high signal-to-noise, high-resolution measurements of disc architectures at submillimetre wavelengths would help refine the relationship between the relative velocities of colliding bodies within these discs and the measured size distribution of the resulting dust grains.

We find no difference in the distributions of dust properties (s_{min}, q) for those systems which are gas-bearing compared to the wider sample. The assumed belt architecture for the systems does not account for the differences in scattered light and millimetre wavelength morphology for the respective dust grain populations. Detailed imaging has demonstrated a diversity of morphologies exist for such systems (e.g. haloes of dust grains, radial separation between the scattered light and millimetre peak surface brightnesses). Overall we may conclude that the impact of the presence of gas on dust properties is therefore weak in general, although perhaps important in the specifics.

We have calculated the dust masses for debris discs within the sample and demonstrate that the measured dust masses are consistent with evolution from observed properties of protoplanetary discs and young debris discs in star forming regions (C. F. Manara et al. 2023). We convert the dust masses into disc masses for the sample following the three power-law model presented in A. V. Krivov & M. C. Wyatt (2021), but substituting their assumed $q = 3.5$ for the q measured in this analysis. The inferred disc masses do not reach the same high levels presented in that work such that, at least under the assumption of a 200 km maximum size for bodies in the disc, the total masses we calculate are consistent with the constraint of gravitational stability for protoplanetary discs (A. Isella, J. M. Carpenter & A. I. Sargent 2009).

Finally, we calculate flux densities for the sample extrapolated from the model fits at infrared to sub-millimetre wavelengths. At millimetre wavelengths, we identify a sub-set of 47 discs amenable to detection or more detailed characterization at millimetre wavelengths. These discs are bright enough to be spatially resolved in a manner consistent with the existing REASONS sample (L. Matrà et al. 2025). These systems are systematically fainter and older than the REASONS sample, and their characterization would reveal a new region of parameter space for disc evolution studies. At centimetre wavelengths, we find that a the size distribution inferred at far-infrared and centimetre wavelengths are not necessarily in tension such that an excess of small grains or discontinuous size distribution is not always necessary to describe centimetre-bright debris discs (M. Kim & S. Wolf 2024). We identify a sub-set of 20 discs bright enough for detection at $\simeq$ centimetre wavelengths, the measurement of which would effectively double the number of such systems observed at SNR ≥ 5 (B. J. Norfolk et al. 2021).

ACKNOWLEDGEMENTS

Facilities: None.

Software: This paper has made use of the Python packages AS-TROPY (Astropy Collaboration et al. 2013, 2018), SCIPY (P. Virtanen et al. 2020), NUMPY (C. R. Harris et al. 2020), MATPLOTLIB (J. D. Hunter 2007), MIEPYTHON (S. Prahl 2024), EMCEE (D. Foreman-Mackey et al. 2013), and CORNER (D. Foreman-Mackey 2016).

DATA AVAILABILITY

The data underlying this article and the scripts used in their analysis are available through the GitHub repository https://github.com/jontymarshall/SEDs_Of_Spatially_Resolved_Discs.

REFERENCES

Akeson R. L., Jensen E. L. N., 2014, ApJ, 784, 62
Akeson R. L., Jensen E. L. N., Carpenter J., Ricci L., Laos E., Nogueira N. F., Suen-Lewis E. M., 2019, ApJ, 872, 158
Andrews S. M., Rosenfeld K. A., Kraus A. L., Wilner D. J., 2013, ApJ, 771, 129
Ansdell M. et al., 2016, ApJ, 828, 46
Ansdell M. et al., 2018, ApJ, 859, 21
Astropy Collaboration et al., 2013, A&A, 558, A33
Astropy Collaboration et al., 2018, AJ, 156, 123
Barenfeld S. A., Carpenter J. M., Ricci L., Isella A., 2016, ApJ, 827, 142
Benz W., Asphaug E., 1999, Icarus, 142, 5
Broekhoven-Fiene H. et al., 2013, ApJ, 762, 52
Bryden G. et al., 2009, ApJ, 705, 1226
Burns J. A., Lamy P. L., Soter S., 1979, Icarus, 40, 1
Cao P.-C., Liu Q., Liao N.-H., Yang Q.-C., Huang D., 2023, Res. Astron. Astrophys., 23, 085002
Carpenter J. M., Ricci L., Isella A., 2014, ApJ, 787, 42
Chen C. H., Mittal T., Kuchner M., Forrest W. J., Lisse C. M., Manoj P., Sargent B. A., Watson D. M., 2014, ApJS, 211, 25
Choquet É. et al., 2018, ApJ, 854, 53
Cleeves L. I., Öberg K. I., Wilner D. J., Huang J., Loomis R. A., Andrews S. M., Czekala I., 2016, ApJ, 832, 110
Cranmer S. R., Wilner D. J., MacGregor M. A., 2013, ApJ, 772, 149
Dohnanyi J. S., 1969, J. Geophys. Res., 74, 2531
Draine B. T., 2003, ARA&A, 41, 241
Eiroa C. et al., 2011, A&A, 536, L4
Eiroa C. et al., 2013, A&A, 555, A11

Ertel S., Wolf S., Metchev S., Schneider G., Carpenter J. M., Meyer M. R., Hillenbrand L. A., Silverstone M. D., 2011, A&A, 533, A132

Ertel S. et al., 2012, A&A, 541, A148

Esposito T. M. et al., 2020, AJ, 160, 24

Farihi J., 2016, New A Rev., 71, 9

Foreman-Mackey D., 2016, J. Open Sour. Soft., 24, 1

Foreman-Mackey D., Hogg D. W., Lang D., Goodman J., 2013, PASP, 125, 306

Gáspár A., Psaltis D., Rieke G. H., Özel F., 2012, ApJ, 754, 74

Gáspár A., Rieke G. H., Balog Z., 2013, ApJ, 768, 25

Harris C. R. et al., 2020, Nature, 585, 357

Hengst S., Marshall J. P., Horner J., Marsden S. C., 2017, MNRAS, 468, 4725

Hengst S., Marshall J. P., Horner J., Marsden S. C., 2020, MNRAS, 497, 1098

Heras A. M., Eiroa C., del Burgo C., Marshall J. P., Montesinos B., 2025, A&A, 694, A325

Holland W. S. et al., 2017, MNRAS, 470, 3606

Horner J. et al., 2020, PASP, 132, 102001

Hughes A. M., Duchêne G., Matthews B. C., 2018, ARA&A, 56, 541

Hunter J. D., 2007, Computing in Science and Engineering, 9, 90

Isella A., Carpenter J. M., Sargent A. I., 2009, ApJ, 701, 260

Ishihara D. et al., 2010, A&A, 514, A1

Kadono T., Kobayashi H., Yokoyama M., 2024, ApJ, 960, 38

Kennedy G. M. et al., 2018, MNRAS, 476, 4584

Kim M., Wolf S., 2024, A&A, 683, A148

Kobayashi H., Tanaka H., 2010, Icarus, 206, 735

Kral Q., Matrà L., Wyatt M. C., Kennedy G. M., 2017, MNRAS, 469, 521

Krivov A. V., 2010, Res. Astron. Astrophys., 10, 383

Krivov A. V., Wyatt M. C., 2021, MNRAS, 500, 718

Krivov A. V., Löhne T., Sremčević M., 2006, A&A, 455, 509

Krivov A. V. et al., 2013, ApJ, 772, 32

Lieman-Sifry J., Hughes A. M., Carpenter J. M., Gorti U., Hales A., Flaherty K. M., 2016, ApJ, 828, 25

Liseau R. et al., 2015, A&A, 573, L4

Lisse C. M. et al., 2012, ApJ, 747, 93

Löhne T., 2020, A&A, 641, A75

Löhne T., Krivov A. V., Rodmann J., 2008, ApJ, 673, 1123

Long F. et al., 2018, ApJ, 869, 17

Long F. et al., 2019, ApJ, 882, 49

MacGregor M. A., Lawler S. M., Wilner D. J., Matthews B. C., Kennedy G. M., Booth M., Di Francesco J., 2016, ApJ, 828, 113

Manara C. F., Ansdell M., Rosotti G. P., Hughes A. M., Armitage P. J., Lodato G., Williams J. P., 2023, eds Inutsuka S., Aikawa Y., Muto T., Tomida K., Tamura M., in Astronomical Society of the Pacific Conference Series, Vol. 534, Protostars and Planets VII. p. 539

Marino S., Flock M., Henning T., Kral Q., Matrà L., Wyatt M. C., 2020, MNRAS, 492, 4409

Marshall J. P. et al., 2013, A&A, 557, A58

Marshall J. P. et al., 2014, A&A, 565, A15

Marshall J. P., Maddison S. T., Thilliez E., Matthews B. C., Wilner D. J., Greaves J. S., Holland W. S., 2017, MNRAS, 468, 2719

Marshall J. P., Milli J., Choquet É., del Burgo C., Kennedy G. M., Matrà L., Ertel S., Boccaletti A., 2018, ApJ, 869, 10

Marshall J. P., Cotton D. V., Scicluna P., Bailey J., Kedziora-Chudczer L., Bott K., 2020, MNRAS, 499, 5915

Marshall J. P., Wang L., Kennedy G. M., Zeegers S. T., Scicluna P., 2021, MNRAS, 501, 6168

Marshall J. P. et al., 2023, MNRAS, 521, 5940

Marshall J. P., Hengst S., Trejo-Cruz A., del Burgo C., Milli J., Booth M., Augereau J. C., Choquet E., Morales F. Y., Thèbault Ph., Kemper F., Faramaz-Gorka V., Bryden G., 2025, MNRAS, 541,71

Matrà L. et al., 2025, A&A, 693, A151

Mittal T., Chen C. H., Jang-Condell H., Manoj P., Sargent B. A., Watson D. M., Lisse C. M., 2015, ApJ, 798, 87

Mohan A., Wedemeyer S., Pandit S., Saberi M., Hauschildt P. H., 2021, A&A, 655, A113

Montesinos B. et al., 2016, A&A, 593, A51

Moór A., Kóspál A., Ábrahám P., Balog Z., Csengeri T., Henning T., Juhász A., Kiss C., 2016, ApJ, 826, 123

Moór A. et al., 2017, ApJ, 849, 123

Morales F. Y., Bryden G., Werner M. W., Stapelfeldt K. R., 2016, ApJ, 831, 97

Najita J. R., Kenyon S. J., Bromley B. C., 2022, ApJ, 925, 45

Norfolk B. J. et al., 2021, MNRAS, 507, 3139

O'Brien D. P., Greenberg R., 2003, Icarus, 164, 334

Pan M., Sari R., 2005, Icarus, 173, 342

Pan M., Schlichting H. E., 2012, ApJ, 747, 113

Pascucci I. et al., 2016, ApJ, 831, 125

Pawellek N., Krivov A. V., 2015, MNRAS, 454, 3207

Pawellek N., Krivov A. V., Marshall J. P., Montesinos B., Ábrahám P., Moór A., Bryden G., Eiroa C., 2014, ApJ, 792, 65

Pawellek N., Moór A., Pascucci I., Krivov A. V., 2019, MNRAS, 487, 5874

Pawellek N. et al., 2024, MNRAS, 527, 3559

Prahl S., Zenodo, 2024, miepython: Pure python calculation of Mie scattering, https://doi.org/10.5281/zenodo.11135148

Ricci L., Testi L., Maddison S. T., Wilner D. J., 2012, A&A, 539, L6

Ricci L., Maddison S. T., Wilner D., MacGregor M. A., Ubach C., Carpenter J. M., Testi L., 2015, ApJ, 813, 138

Sanchis E. et al., 2020, A&A, 633, A114

Schüppler C. et al., 2015, A&A, 581, A97

Steele A., Hughes A. M., Carpenter J., Ricarte A., Andrews S. M., Wilner D. J., Chiang E., 2016, ApJ, 816, 27

Stuber T. A., Wolf S., 2022, A&A, 658, A121

Su K. Y. L. et al., 2006, ApJ, 653, 675

Sylvester R. J., Barlow M. J., Skinner C. J., 1994, Ap&SS, 212, 261

Tanaka H., Inaba S., Nakazawa K., 1996, Icarus, 123, 450

Terrill J., Marino S., Booth R. A., Han Y., Jennings J., Wyatt M. C., 2023, MNRAS, 524, 1229

Thébault P., Augereau J. C., 2007, A&A, 472, 169

Thebault P., Kral Q., 2019, A&A, 626, A24

Thureau N. D. et al., 2014, MNRAS, 445, 2558

Tsukagoshi T. et al., 2019, ApJ, 871, 5

van der Plas G. et al., 2016, ApJ, 819, 102

Villenave M. et al., 2021, A&A, 653, A46

Virtanen P. et al., 2020, Nature Methods, 17, 261

Ward-Duong K. et al., 2018, AJ, 155, 54

Wenger M. et al., 2000, A&AS, 143, 9

White J. A., Aufdenberg J., Boley A. C., Hauschildt P., Hughes M., Matthews B., Wilner D., 2018, ApJ, 859, 102

Williams J. P., Cieza L., Hales A., Ansdell M., Ruiz-Rodriguez D., Casassus S., Perez S., Zurlo A., 2019, ApJ, 875, L9

Wright E. L. et al., 2010, AJ, 140, 1868

Wyatt M. C., Smith R., Su K. Y. L., Rieke G. H., Greaves J. S., Beichman C. A., Bryden G., 2007, ApJ, 663, 365

Wyatt M. C., Clarke C. J., Booth M., 2011, Celestial Mech. Dyn. Astron., 111, 1

Xie C. et al., 2025, Nature, 641, 608

Yelverton B., Kennedy G. M., Su K. Y. L., Wyatt M. C., 2019, MNRAS, 488, 3588

APPENDIX A: DATA TABLE

Here, we provide the source properties for the 133 debris discs with well-modelled SEDs along with the calculated values for their dust properties, namely s_{min}, q, and M_{dust}.

Table A1. Source parameters for the debris discs ($L_\star$, R_{disc}, σ_{disc}, s_{blow}) and the dust properties derived from radiative transfer modelling (s_{min}, q, M_{dust}, M_{disc}). Systems with a warm inner component to their disc are denoted by a † symbol next to the name. We also include predicted flux densities for $\lambda_{obs} = 1.3$ and 7 mm (ALMA B6 and B1), based on the maximum amplitude probability model. Potentially observable systems in B6, shown in Fig. 8, have predicted flux densities consistent with 300 μJy, while potentially observable systems in B1 have predicted flux densities consistent with 15 μJy.

Name	Luminosity ($L_\odot$)	Mass ($M_\odot$)	R_{disc} (au)	FWHM (au)	s_{blow} (μm)	s_{min} (μm)	q	M_{dust} ($10^{-3}M_\oplus$)	M_{disc} ($M_\oplus$)	$F_{B6,pred}$ (mJy)	$F_{B1,pred}$ (μJy)
HD216956C	0.005	0.219	26	≤ 8	–	$10.88^{+2.77}_{-3.81}$	$3.9^{+0.3}_{-0.2}$	$1.9^{+0.3}_{-0.4}$	$2.8^{+16.1}_{-7.1}$	$0.263^{0.047}_{0.053}$	$1.2^{0.2}_{0.2}$
GJ581	0.012	0.283	25^{+3}_{-7}	19^{+3}_{-8}	–	$2.88^{+1.53}_{-1.51}$	3.5	$0.7^{+0.1}_{-0.1}$	$7.3^{+1.0}_{-0.7}$	$0.276^{0.037}_{0.027}$	$2.3^{0.2}_{0.2}$
GJ3760	0.049	0.421	59^{+9}_{-15}	34^{+14}_{-16}	–	$7.50^{+1.34}_{-3.70}$	3.5	$13.6^{+4.9}_{-1.8}$	$148.9^{+53.4}_{-19.7}$	$2.718^{0.974}_{0.359}$	$17.6^{6.3}_{2.3}$
HD197481	0.096	0.512	34^{+0}_{0}	12^{+0}_{-0}	–	$0.13^{+0.64}_{-0.10}$	$3.1^{+0.1}_{-0.1}$	$6.7^{+2.0}_{-1.4}$	$138.0^{+51.3}_{-35.8}$	$6.651^{1.991}_{1.416}$	$60.6^{17.8}_{12.6}$
GJ14	0.109	0.531	99^{+3}_{-8}	33^{+7}_{-8}	–	$7.86^{+2.16}_{-4.68}$	$3.4^{+0.2}_{-0.2}$	$1.1^{+0.1}_{-0.1}$	$13.9^{+6.9}_{-5.1}$	$1.854^{0.232}_{0.193}$	$13.0^{1.6}_{1.3}$
TWA7	0.127	0.555	90^{+20}_{-20}	90^{+20}_{-20}	–	$0.12^{+0.35}_{-0.09}$	$3.6^{+0.0}_{-0.1}$	$48.4^{+61.9}_{-22.8}$	$435.8^{+678.5}_{-243.2}$	$0.924^{1.176}_{0.432}$	$5.8^{7.1}_{2.6}$
TYC93404371	0.191	0.623	130^{+20}_{-60}	100^{+40}_{-60}	–	$0.64^{+2.78}_{-0.58}$	$3.3^{+0.1}_{-0.2}$	$13.7^{+9.3}_{-4.4}$	$201.7^{+208.7}_{-107.8}$	$3.625^{2.467}_{1.155}$	$25.6^{17.3}_{8.1}$
HD128311	0.288	0.700	50^{+5}_{-15}	30^{+11}_{-15}	–	$4.16^{+4.30}_{-3.21}$	3.5	$0.3^{+0.2}_{-0.1}$	$3.7^{+2.6}_{-0.8}$	$0.169^{0.105}_{0.033}$	$1.5^{0.6}_{0.2}$
HD23356	0.298	0.708	60^{+5}_{-9}	18^{+9}_{-9}	–	$5.74^{+19.74}_{-4.88}$	3.5	$0.2^{+0.1}_{-0.0}$	$1.7^{+1.4}_{-0.4}$	$0.163^{0.111}_{0.029}$	$1.7^{0.6}_{0.2}$
HD192263	0.304	0.711	85^{+4}_{-6}	16^{+8}_{-6}	–	$0.26^{+0.94}_{-0.23}$	3.5	$1.0^{+1.7}_{-0.4}$	$11.2^{+18.4}_{-4.3}$	$0.170^{0.261}_{0.062}$	$1.4^{1.6}_{0.4}$
HD22049†	0.337	0.733	68^{+0}_{-1}	12^{+1}_{-1}	–	$0.51^{+3.28}_{-0.46}$	$3.2^{+0.1}_{-0.1}$	$0.6^{+0.3}_{-0.2}$	$10.5^{+7.3}_{-4.0}$	$15.176^{8.267}_{3.992}$	$120.9^{58.4}_{28.2}$
HD89452	0.366	0.750	69^{+7}_{-13}	35^{+13}_{-13}	–	$6.98^{+1.40}_{-3.13}$	3.5	$4.7^{+1.0}_{-0.3}$	$51.3^{+11.0}_{-3.4}$	$0.928^{0.197}_{0.062}$	$5.9^{1.2}_{0.4}$
HD92945	0.367	0.751	96^{+1}_{-3}	80^{+3}_{-3}	–	$5.95^{+1.57}_{-1.96}$	$3.8^{+0.1}_{-0.1}$	$7.4^{+1.0}_{-0.6}$	$29.1^{+26.3}_{-19.7}$	$2.677^{0.353}_{0.230}$	$12.0^{1.5}_{1.0}$
HD17925	0.399	0.769	25^{+2}_{-4}	8^{+4}_{-4}	–	$0.21^{+6.89}_{-0.19}$	$3.2^{+0.8}_{-0.3}$	$0.4^{+0.5}_{-0.1}$	$7.3^{+24.3}_{-4.2}$	$0.269^{0.256}_{0.083}$	$3.6^{2.0}_{0.7}$
HD23484	0.408	0.774	49^{+4}_{-18}	39^{+4}_{-18}	–	$4.37^{+2.47}_{-2.05}$	3.5	$1.1^{+0.2}_{-0.1}$	$11.6^{+2.5}_{-1.5}$	$0.618^{0.129}_{0.078}$	$3.9^{0.7}_{0.4}$
HD158633	0.415	0.778	33^{+6}_{-6}	25^{+3}_{-6}	–	$5.29^{+2.65}_{-3.01}$	$4.1^{+0.6}_{-0.5}$	$0.3^{+3.8}_{-0.1}$	$0.7^{+3.8}_{-0.7}$	$0.058^{0.010}_{0.005}$	$1.2^{0.0}_{0.0}$
HD131511	0.517	0.828	33^{+9}_{-5}	9^{+5}_{-5}	–	$7.25^{+38.91}_{-7.11}$	3.5	$0.1^{+0.3}_{-0.0}$	$0.7^{+3.0}_{-0.2}$	$0.104^{0.207}_{0.017}$	$2.4^{1.2}_{0.1}$
HD31392	0.563	0.848	126^{+3}_{-24}	104^{+8}_{-24}	–	$2.35^{+0.94}_{-0.97}$	3.5	$1.7^{+0.2}_{-0.2}$	$18.2^{+2.5}_{-1.9}$	$1.094^{0.149}_{0.115}$	$6.4^{0.8}_{0.6}$
HD53143	0.588	0.859	88^{+0}_{-2}	23^{+2}_{-2}	–	$0.66^{+0.98}_{-0.58}$	$3.4^{+0.1}_{-0.1}$	$3.5^{+2.1}_{-0.8}$	$44.9^{+38.4}_{-16.9}$	$1.867^{1.115}_{0.402}$	$11.6^{6.5}_{2.4}$
HD61005†	0.631	0.877	72^{+0}_{-1}	38^{+1}_{-1}	–	$4.10^{+3.06}_{-2.27}$	$3.5^{+0.2}_{-0.2}$	$23.2^{+6.1}_{-4.8}$	$236.2^{+174.6}_{-125.5}$	$3.860^{1.019}_{0.800}$	$20.9^{5.5}_{4.3}$
HD166	0.634	0.878	27^{+3}_{-3}	14^{+5}_{-3}	–	$2.49^{+2.48}_{-1.23}$	$3.8^{+0.3}_{-0.3}$	$0.9^{+0.2}_{-0.2}$	$3.5^{+6.9}_{-4.6}$	$0.106^{0.018}_{0.024}$	$1.6^{0.1}_{0.1}$
HD20794	0.646	0.883	32^{+3}_{-5}	9^{+5}_{-5}	–	$0.50^{+15.49}_{-0.47}$	3.5	$0.1^{+0.2}_{-0.1}$	$0.7^{+2.3}_{-0.6}$	$0.231^{0.142}_{0.035}$	$7.2^{0.7}_{0.2}$
HD48370	0.774	0.929	88^{+7}_{-11}	37^{+4}_{-12}	–	$1.93^{+31.74}_{-1.72}$	$2.7^{+0.5}_{-0.4}$	$4.8^{+2.0}_{-1.3}$	$133.7^{+131.6}_{-67.5}$	$6.683^{2.748}_{1.783}$	$72.5^{29.7}_{19.3}$
HD115617	0.831	0.949	47^{+1}_{-4}	36^{+4}_{-4}	–	$0.37^{+3.96}_{-0.34}$	$3.0^{+0.2}_{-0.2}$	$0.3^{+0.2}_{-0.1}$	$7.2^{+5.0}_{-2.6}$	$1.980^{0.889}_{0.468}$	$20.2^{7.5}_{3.9}$
HD38858	0.843	0.952	110^{+10}_{-20}	80^{+30}_{-20}	–	$0.54^{+3.09}_{-0.50}$	$3.3^{+0.1}_{-0.2}$	$1.3^{+1.0}_{-0.4}$	$19.3^{+20.5}_{-9.2}$	$2.675^{2.167}_{0.759}$	$17.8^{13.6}_{4.7}$
HD30495	0.971	0.992	29^{+4}_{-4}	22^{+3}_{-5}	–	$3.78^{+2.61}_{-1.83}$	3.5	$0.4^{+0.2}_{-0.1}$	$4.9^{+1.7}_{-1.0}$	$0.257^{0.070}_{0.042}$	$3.1^{0.4}_{0.2}$
HD202628	0.982	0.995	155^{+0}_{-3}	16^{+3}_{-3}	–	$6.36^{+1.16}_{-1.71}$	$3.8^{+0.1}_{-0.1}$	$1.2^{+0.1}_{-0.1}$	$6.5^{+3.1}_{-2.4}$	$1.052^{0.099}_{0.063}$	$5.5^{0.5}_{0.3}$
HD107146†	0.998	1.000	107^{+0}_{0}	110^{+1}_{-1}	–	$2.68^{+1.45}_{-1.31}$	$3.4^{+0.1}_{-0.1}$	$11.4^{+1.8}_{-1.5}$	$158.7^{+53.0}_{-40.0}$	$11.341^{1.792}_{1.473}$	$72.4^{11.4}_{9.3}$
HD73350	1.009	1.002	100^{+5}_{-18}	85^{+4}_{-18}	–	$2.99^{+3.04}_{-1.35}$	3.5	$1.7^{+0.4}_{-0.3}$	$18.0^{+4.7}_{-3.8}$	$1.230^{0.315}_{0.256}$	$7.7^{1.8}_{1.5}$
HD202206	1.075	1.021	83^{+13}_{-16}	39^{+21}_{-17}	0.38	$6.27^{+1.97}_{-2.19}$	3.5	$1.2^{+0.2}_{-0.1}$	$12.7^{+1.9}_{-1.1}$	$0.248^{0.036}_{0.021}$	$1.6^{0.2}_{0.1}$
HD110897	1.116	1.032	63^{+5}_{-12}	36^{+16}_{-13}	0.40	$2.99^{+3.17}_{-1.93}$	3.5	$0.3^{+0.2}_{-0.1}$	$3.6^{+1.9}_{-0.8}$	$0.260^{0.120}_{0.053}$	$2.5^{0.7}_{0.3}$
HD377†	1.175	1.047	80^{+10}_{-10}	20^{+20}_{-10}	0.43	$11.04^{+39.94}_{-10.02}$	$3.5^{+0.8}_{-1.5}$	$3.7^{+2.3}_{-1.3}$	$39.0^{+128.9}_{-92.0}$	$1.332^{0.832}_{0.460}$	$6.9^{4.2}_{2.3}$
HD45184	1.176	1.047	77^{+5}_{-31}	64^{+3}_{-32}	0.43	$2.27^{+1.49}_{-0.99}$	3.5	$1.1^{+0.2}_{-0.2}$	$11.5^{+2.4}_{-2.0}$	$0.595^{0.121}_{0.101}$	$3.9^{0.6}_{0.5}$
HD104860	1.180	1.048	110	≤ 200	0.43	$4.21^{+3.93}_{-2.69}$	$3.5^{+0.2}_{-0.2}$	$6.7^{+2.5}_{-1.5}$	$67.3^{+63.1}_{-37.6}$	$2.714^{1.019}_{0.591}$	$15.0^{5.6}_{3.2}$
HD207129	1.218	1.058	150^{+2}_{-6}	39^{+7}_{-6}	0.45	$1.39^{+1.52}_{-1.09}$	$3.6^{+0.1}_{-0.1}$	$1.5^{+0.6}_{-0.3}$	$14.0^{+10.7}_{-6.1}$	$2.146^{0.799}_{0.393}$	$13.1^{4.3}_{2.1}$
HD187897	1.231	1.061	90^{+10}_{-9}	27^{+33}_{-10}	0.45	$2.94^{+0.94}_{-0.86}$	3.5	$1.0^{+0.1}_{-0.1}$	$10.4^{+1.1}_{-1.0}$	$0.316^{0.033}_{0.031}$	$2.1^{0.2}_{0.2}$
HD1461	1.239	1.063	88^{+5}_{-8}	28^{+27}_{-9}	0.46	$3.79^{+2.18}_{-1.29}$	3.5	$0.5^{+0.1}_{-0.1}$	$5.2^{+1.0}_{-0.9}$	$0.347^{0.061}_{0.057}$	$2.7^{0.3}_{0.3}$
HD105	1.254	1.067	85	≤ 30	0.47	$3.42^{+2.43}_{-1.26}$	$3.2^{+0.1}_{-0.1}$	$3.4^{+0.3}_{-0.3}$	$59.8^{+13.7}_{-12.2}$	$1.804^{0.172}_{0.176}$	$15.0^{1.4}_{1.4}$
HD38397	1.363	1.093	94^{+14}_{-7}	34^{+18}_{-7}	0.52	$10.16^{+39.82}_{-7.23}$	3.5	$5.8^{+2.5}_{-1.3}$	$63.1^{+27.7}_{-14.1}$	$1.376^{0.602}_{0.307}$	$8.0^{3.4}_{1.7}$
HD50554	1.499	1.123	75^{+5}_{-12}	30^{+14}_{-13}	0.59	$2.12^{+1.05}_{-0.95}$	3.5	$0.6^{+0.2}_{-0.1}$	$6.8^{+1.7}_{-1.0}$	$0.161^{0.038}_{0.023}$	$1.3^{0.2}_{0.1}$
HD82943	1.531	1.130	89^{+6}_{-21}	62^{+14}_{-22}	0.60	$3.78^{+2.52}_{-1.41}$	3.5	$1.3^{+0.2}_{-0.2}$	$13.7^{+2.4}_{-2.0}$	$0.750^{0.127}_{0.106}$	$4.8^{0.7}_{0.6}$
HD10647†	1.545	1.132	100^{+2}_{-6}	70^{+5}_{-6}	0.61	$2.90^{+2.58}_{-1.42}$	$3.6^{+0.1}_{-0.1}$	$3.3^{+0.8}_{-0.7}$	$32.0^{+19.2}_{-14.5}$	$4.164^{1.042}_{0.812}$	$23.4^{5.5}_{4.3}$
HD48682	1.857	1.194	93^{+3}_{-12}	83^{+1}_{-12}	0.77	$0.35^{+2.50}_{-0.31}$	$3.3^{+0.1}_{-0.1}$	$1.3^{+1.2}_{-0.6}$	$19.3^{+22.4}_{-10.8}$	$1.873^{1.602}_{0.800}$	$14.3^{10.8}_{5.4}$
HD219482	1.907	1.203	44^{+4}_{-6}	12^{+6}_{-6}	0.80	$1.30^{+1.68}_{-0.80}$	3.5	$0.5^{+0.2}_{-0.1}$	$4.9^{+2.5}_{-1.6}$	$0.130^{0.048}_{0.030}$	$1.8^{0.2}_{0.2}$

Table A1 – *continued*

Name	Luminosity (L⊙)	Mass (M⊙)	$R_{\rm disc}$ (au)	FWHM (au)	$s_{\rm blow}$ (μm)	$s_{\rm min}$ (μm)	q	$M_{\rm dust}$ (10^{-3}M⊕)	$M_{\rm disc}$ (M⊕)	$F_{\rm B6,pred}$ (mJy)	$F_{\rm B1,pred}$ (μJy)
HD8907	1.972	1.214	100^{+3}_{-22}	49^{+8}_{-22}	0.83	$4.77^{+1.69}_{-1.05}$	$3.4^{+0.1}_{-0.1}$	$3.0^{+0.2}_{-0.2}$	$39.9^{+7.3}_{-7.2}$	$2.192^{0.140}_{0.151}$	$13.0^{0.8}_{0.9}$
HD165908	2.144	1.243	130^{+5}_{-15}	113^{+3}_{-15}	0.93	$7.60^{+8.46}_{-7.38}$	$3.6^{+0.4}_{-1.2}$	$0.2^{+0.1}_{-0.0}$	$1.7^{+3.8}_{-4.2}$	$0.884^{0.517}_{0.130}$	$7.2^{2.8}_{0.7}$
HD52265	2.263	1.263	124^{+2}_{-16}	85^{+14}_{-16}	1.0	$0.81^{+0.90}_{-0.71}$	3.5	$0.4^{+0.5}_{-0.3}$	$4.0^{+5.5}_{-1.0}$	$0.166^{0.202}_{0.037}$	$1.6^{1.2}_{0.2}$
HD35841	2.363	1.279	57^{+3}_{-8}	15^{+9}_{-8}	1.1	$2.59^{+11.67}_{-2.36}$	$3.1^{+0.4}_{-0.5}$	$17.3^{+5.9}_{-4.6}$	$321.2^{+290.0}_{-214.0}$	$0.917^{0.314}_{0.243}$	$6.4^{2.2}_{1.7}$
HD111520	2.654	1.322	76^{+6}_{-30}	50^{+20}_{-30}	1.2	$0.47^{+0.57}_{-0.42}$	$3.2^{+0.1}_{-0.1}$	$28.3^{+6.6}_{-3.1}$	$515.0^{+181.0}_{-110.6}$	$1.469^{0.343}_{0.161}$	$10.3^{2.4}_{1.1}$
HD146181	2.699	1.328	74	≤90	1.2	$1.18^{+0.85}_{-0.99}$	$3.3^{+0.2}_{-0.2}$	$26.8^{+7.0}_{-4.6}$	$394.2^{+217.5}_{-141.8}$	$0.935^{0.245}_{0.159}$	$5.9^{1.5}_{0.9}$
HD191089	2.740	1.334	44^{+0}_{-3}	16^{+3}_{-3}	1.3	$0.96^{+0.43}_{-0.50}$	$3.2^{+0.1}_{-0.1}$	$18.0^{+1.7}_{-1.0}$	$316.8^{+61.4}_{-43.9}$	$2.134^{0.197}_{0.116}$	$16.2^{1.5}_{0.9}$
HD189002	2.806	1.343	592^{+11}_{-136}	469^{+38}_{-136}	1.3	$0.58^{+4.69}_{-0.53}$	3.5	$11.2^{+28.8}_{-6.7}$	$122.1^{+314.3}_{-73.3}$	$1.600^{4.116}_{0.960}$	$9.2^{23.5}_{5.5}$
HD206893	2.852	1.349	108^{+4}_{-10}	100^{+10}_{-10}	1.3	$6.42^{+2.52}_{-1.68}$	$3.6^{+0.1}_{-0.2}$	$3.0^{+0.3}_{-0.2}$	$25.7^{+10.0}_{-12.6}$	$1.365^{0.121}_{0.101}$	$7.6^{0.6}_{0.5}$
HD181327	2.883	1.353	81^{+0}_{0}	16^{+0}_{-1}	1.4	$1.04^{+0.89}_{-0.76}$	$3.1^{+0.1}_{-0.1}$	$30.6^{+5.3}_{-4.2}$	$578.1^{+196.2}_{-163.5}$	$11.336^{1.966}_{1.575}$	$89.4^{15.5}_{12.4}$
HD127821	2.949	1.362	120	≤300	1.4	$5.69^{+2.21}_{-2.86}$	$3.8^{+0.2}_{-0.1}$	$2.2^{+0.5}_{-0.2}$	$7.8^{+12.4}_{-7.0}$	$1.772^{0.386}_{0.170}$	$7.7^{1.5}_{0.7}$
HD129590	2.973	1.365	79^{+4}_{-30}	70^{+20}_{-30}	1.4	$1.15^{+0.52}_{-0.67}$	$3.4^{+0.1}_{-0.1}$	$75.0^{+14.8}_{-8.5}$	$952.9^{+416.1}_{-258.5}$	$1.473^{0.291}_{0.166}$	$8.5^{1.7}_{1.0}$
HD112810†	3.145	1.387	90	≤200	1.5	$4.34^{+0.72}_{-0.53}$	$3.6^{+0.1}_{-0.1}$	$10.0^{+0.7}_{-0.7}$	$92.4^{+21.6}_{-20.5}$	$0.517^{0.038}_{0.035}$	$2.6^{0.2}_{0.2}$
HD22484	3.148	1.388	46^{+4}_{-8}	15^{+8}_{-8}	1.5	$1.06^{+1.69}_{-0.94}$	3.5	$0.2^{+0.4}_{-0.1}$	$2.2^{+4.0}_{-0.8}$	$0.239^{0.183}_{0.035}$	$5.7^{1.0}_{0.2}$
HD145560†	3.221	1.397	76^{+4}_{-20}	50^{+20}_{-20}	1.6	$19.96^{+47.22}_{-18.49}$	$3.5^{+0.8}_{-1.3}$	$17.8^{+8.5}_{-6.3}$	$188.9^{+530.6}_{-396.5}$	$1.231^{0.591}_{0.439}$	$6.4^{3.1}_{2.3}$
HD164249	3.241	1.399	62^{+3}_{-10}	20^{+10}_{-10}	1.6	$4.22^{+0.50}_{-0.53}$	$3.6^{+0.1}_{-0.1}$	$12.2^{+0.9}_{-1.1}$	$105.5^{+38.5}_{-35.7}$	$1.097^{0.081}_{0.096}$	$5.3^{0.4}_{0.4}$
HD146897	3.352	1.413	82	≤90	1.6	$0.88^{+0.72}_{-0.74}$	$3.5^{+0.1}_{-0.2}$	$92.9^{+44.7}_{-15.6}$	$966.8^{+884.9}_{-434.0}$	$1.313^{0.631}_{0.220}$	$7.3^{3.5}_{1.2}$
HD50571	3.362	1.414	190^{+20}_{-30}	160^{+30}_{-30}	1.7	$4.60^{+2.36}_{-2.08}$	$3.6^{+0.1}_{-0.1}$	$1.2^{+0.2}_{-0.1}$	$10.9^{+5.9}_{-4.3}$	$1.551^{0.265}_{0.173}$	$7.9^{1.2}_{0.8}$
HD139664	3.386	1.417	75^{+6}_{-10}	60^{+10}_{-10}	1.7	$1.26^{+1.83}_{-1.07}$	$3.4^{+0.2}_{-0.1}$	$1.7^{+0.7}_{-0.5}$	$22.2^{+18.2}_{-9.8}$	$2.182^{0.908}_{0.566}$	$14.5^{5.2}_{3.2}$
HD205674	3.456	1.425	160^{+10}_{-20}	120^{+20}_{-20}	1.7	$3.47^{+0.44}_{-0.27}$	$3.6^{+0.1}_{-0.1}$	$4.3^{+0.3}_{-0.3}$	$37.5^{+7.8}_{-8.7}$	$1.211^{0.071}_{0.074}$	$7.0^{0.4}_{0.4}$
HD216435	3.546	1.436	68^{+8}_{-16}	46^{+11}_{-16}	1.8	$5.75^{+6.75}_{-4.53}$	3.5	$0.2^{+0.2}_{-0.0}$	$2.7^{+1.9}_{-0.5}$	$0.132^{0.071}_{0.018}$	$1.6^{0.4}_{0.1}$
HD170773	3.579	1.439	194^{+2}_{-5}	68^{+5}_{-5}	1.8	$5.74^{+1.39}_{-1.32}$	$3.6^{+0.1}_{-0.1}$	$5.8^{+0.4}_{-0.3}$	$52.7^{+12.7}_{-12.2}$	$6.288^{0.456}_{0.377}$	$33.6^{2.4}_{2.0}$
HD15115†	3.712	1.455	93^{+1}_{-7}	21^{+6}_{-7}	1.9	$7.03^{+8.60}_{-3.97}$	$3.4^{+0.2}_{-0.3}$	$4.5^{+1.2}_{-0.9}$	$61.1^{+41.7}_{-36.4}$	$1.867^{0.480}_{0.362}$	$12.6^{3.2}_{2.4}$
HD114082	3.788	1.463	38	≤40	1.9	$1.32^{+0.71}_{-0.84}$	$3.5^{+0.2}_{-0.1}$	$41.5^{+7.4}_{-4.8}$	$496.9^{+262.2}_{-156.7}$	$0.621^{0.110}_{0.072}$	$3.5^{0.6}_{0.4}$
HD142446†	3.869	1.472	110^{+30}_{-40}	80^{+50}_{-40}	2.0	$18.31^{+37.13}_{-13.57}$	$3.8^{+0.5}_{-1.3}$	$7.2^{+1.8}_{-1.5}$	$27.9^{+97.3}_{-171.5}$	$0.378^{0.095}_{0.077}$	$1.4^{0.3}_{0.3}$
HD113337	4.113	1.498	79^{+6}_{-3}	30^{+17}_{-4}	2.1	$10.00^{+1.92}_{-1.90}$	3.5	$1.1^{+0.1}_{-0.0}$	$11.5^{+0.7}_{-0.5}$	$0.609^{0.034}_{0.027}$	$4.0^{0.2}_{0.1}$
HD15745†	4.205	1.507	65^{+6}_{-20}	50^{+10}_{-20}	2.2	$14.15^{+44.22}_{-12.86}$	$3.4^{+1.1}_{-1.5}$	$6.4^{+2.1}_{-1.7}$	$89.9^{+233.2}_{-172.8}$	$1.264^{0.425}_{0.346}$	$8.4^{2.8}_{2.3}$
HD147137†	4.345	1.522	120^{+80}_{-50}	100^{+60}_{-50}	2.3	$17.56^{+42.37}_{-10.95}$	$3.7^{+0.5}_{-1.3}$	$5.6^{+1.0}_{-0.7}$	$32.6^{+75.4}_{-141.2}$	$0.372^{0.063}_{0.048}$	$1.6^{0.3}_{0.2}$
HD113556†	4.386	1.526	110	≤400	2.3	$3.62^{+5.03}_{-0.77}$	$4.3^{+0.4}_{-1.1}$	$7.1^{+1.9}_{-1.6}$	$7.1^{+31.7}_{-7.1}$	$0.136^{0.035}_{0.030}$	$0.4^{0.1}_{0.1}$
HD176894	4.550	1.542	316^{+19}_{-36}	124^{+63}_{-36}	2.4	$14.06^{+44.50}_{-7.00}$	3.5	$2.2^{+0.8}_{-0.5}$	$23.9^{+8.3}_{-5.2}$	$2.122^{0.734}_{0.461}$	$13.1^{4.5}_{2.8}$
HD115600	4.798	1.565	90	≤200	2.6	$0.54^{+0.34}_{-0.36}$	$3.8^{+0.1}_{-0.1}$	$25.3^{+8.9}_{-3.2}$	$109.5^{+140.7}_{-80.9}$	$0.211^{0.073}_{0.026}$	$0.8^{0.3}_{0.1}$
HD109085†	5.042	1.588	153^{+2}_{-3}	53^{+2}_{-3}	2.8	$1.87^{+34.69}_{-1.82}$	$2.4^{+0.3}_{-0.4}$	$0.2^{+0.0}_{-0.0}$	$8.4^{+2.3}_{-2.4}$	$6.462^{0.540}_{0.466}$	$83.9^{6.8}_{5.9}$
HD16743†	5.113	1.594	159^{+2}_{-9}	80^{+8}_{-9}	2.8	$4.71^{+1.23}_{-0.93}$	$3.7^{+0.1}_{-0.1}$	$4.0^{+0.5}_{-0.4}$	$43.5^{+4.9}_{-4.7}$	$1.757^{0.198}_{0.189}$	$9.2^{1.0}_{1.0}$
HD117214	5.572	1.634	42	≤50	3.2	$0.55^{+1.56}_{-0.52}$	$3.3^{+0.1}_{-0.2}$	$32.5^{+17.3}_{-7.7}$	$492.1^{+396.7}_{-228.8}$	$0.714^{0.378}_{0.169}$	$4.1^{2.1}_{0.9}$
HD37594	5.646	1.640	131^{+9}_{-4}	35^{+63}_{-4}	3.2	$5.22^{+2.13}_{-1.27}$	3.5	$2.6^{+0.3}_{-0.3}$	$28.0^{+3.5}_{-3.5}$	$1.738^{0.217}_{0.217}$	$9.1^{1.1}_{1.1}$
HD218396†	5.695	1.644	290^{+10}_{-30}	250^{+30}_{-30}	3.3	$5.63^{+4.13}_{-4.12}$	$3.6^{+0.3}_{-0.3}$	$3.5^{+0.9}_{-0.6}$	$29.7^{+32.9}_{-25.1}$	$6.679^{1.808}_{1.151}$	$34.6^{9.2}_{5.9}$
HD106906	6.578	1.713	100^{+10}_{-40}	80^{+30}_{-40}	3.9	$1.25^{+0.49}_{-0.72}$	$3.6^{+0.2}_{-0.1}$	$15.0^{+2.5}_{-1.9}$	$120.3^{+87.9}_{-49.5}$	$0.377^{0.061}_{0.047}$	$1.8^{0.3}_{0.2}$
HD95086	6.605	1.715	206^{+2}_{-3}	180^{+4}_{-3}	3.9	$1.81^{+0.70}_{-0.94}$	$3.5^{+0.1}_{-0.2}$	$15.2^{+3.7}_{-3.0}$	$179.3^{+104.8}_{-75.4}$	$3.740^{0.913}_{0.726}$	$23.5^{5.7}_{4.5}$
HD27290	6.671	1.720	80^{+4}_{-8}	71^{+1}_{-8}	4.0	$0.60^{+13.15}_{-0.56}$	$2.9^{+0.7}_{-0.3}$	$0.3^{+0.1}_{-0.0}$	$7.2^{+9.3}_{-2.7}$	$1.842^{0.747}_{0.293}$	$17.9^{6.4}_{2.5}$
HD105211†	6.790	1.729	131^{+0}_{-5}	23^{+4}_{-5}	4.1	$7.94^{+42.37}_{-4.99}$	$3.6^{+0.2}_{-1.3}$	$0.7^{+0.1}_{-0.1}$	$6.6^{+4.6}_{-18.8}$	$2.359^{0.404}_{0.303}$	$14.5^{2.0}_{1.5}$
HD38529	6.892	1.736	108^{+7}_{-23}	54^{+25}_{-23}	4.2	$2.23^{+3.98}_{-1.83}$	3.5	$0.4^{+0.4}_{-0.1}$	$4.7^{+4.6}_{-1.5}$	$0.190^{0.145}_{0.047}$	$2.3^{0.8}_{0.2}$
HD121191†	7.198	1.758	55^{+4}_{-11}	54^{+8}_{-11}	4.4	$1.75^{+0.81}_{-1.17}$	$3.5^{+0.2}_{-0.2}$	$23.0^{+5.9}_{-4.9}$	$242.8^{+203.6}_{-115.3}$	$0.313^{0.080}_{0.066}$	$1.8^{0.4}_{0.4}$
HD10638	7.276	1.763	160	≤400	4.5	$2.71^{+1.93}_{-0.51}$	$3.8^{+0.1}_{-0.2}$	$5.6^{+1.1}_{-0.8}$	$27.1^{+20.1}_{-23.7}$	$1.243^{0.233}_{0.175}$	$5.3^{0.9}_{0.7}$
HD32297†	7.366	1.769	122^{+3}_{-3}	62^{+4}_{-3}	4.5	$1.21^{+0.67}_{-0.92}$	$3.3^{+0.1}_{-0.1}$	$62.7^{+13.3}_{-10.3}$	$913.5^{+431.7}_{-304.2}$	$3.890^{0.826}_{0.641}$	$23.9^{5.1}_{3.9}$
HD195627†	7.877	1.803	119^{+8}_{-46}	107^{+0}_{-47}	4.9	$5.86^{+1.83}_{-2.27}$	$3.4^{+0.2}_{-0.2}$	$1.2^{+0.1}_{-0.1}$	$15.2^{+6.0}_{-4.7}$	$2.712^{0.287}_{0.183}$	$18.3^{1.8}_{1.1}$
HD84870	8.044	1.814	260^{+50}_{-60}	260^{+60}_{-60}	5.1	$2.44^{+0.39}_{-0.38}$	$3.6^{+0.1}_{-0.1}$	$6.7^{+0.6}_{-0.6}$	$64.4^{+17.8}_{-16.5}$	$1.962^{0.168}_{0.165}$	$9.7^{0.8}_{0.8}$

Table A1 – *continued*

Name	Luminosity (L$_\odot$)	Mass (M$_\odot$)	$R_{\rm disc}$ (au)	FWHM (au)	$s_{\rm blow}$ (μm)	$s_{\rm min}$ (μm)	q	$M_{\rm dust}$ (10^{-3}M$_\oplus$)	$M_{\rm disc}$ (M$_\oplus$)	$F_{\rm B6,pred}$ (mJy)	$F_{\rm B1,pred}$ (μJy)
HD110058	8.308	1.831	50	≤100	5.3	$0.71^{+0.49}_{-0.54}$	$3.4^{+0.1}_{-0.1}$	$32.4^{+6.2}_{-3.3}$	$415.6^{+181.6}_{-109.8}$	$0.664^{0.128}_{0.067}$	$3.8^{0.7}_{0.4}$
HD39060†	8.391	1.836	105^{+1}_{-3}	92^{+3}_{-3}	5.4	$1.07^{+0.46}_{-0.46}$	$3.6^{+0.1}_{-0.1}$	$24.4^{+4.5}_{-3.5}$	$193.8^{+86.5}_{-72.4}$	$17.904^{3.316}_{2.545}$	$85.9^{15.5}_{11.9}$
HD30422	8.480	1.842	103^{+15}_{-25}	55^{+24}_{-26}	5.4	$2.71^{+0.69}_{-0.82}$	3.5	$0.6^{+0.1}_{-0.1}$	$6.4^{+0.8}_{-0.9}$	$0.132^{0.016}_{0.017}$	$1.0^{0.1}_{0.1}$
HD95698	8.680	1.854	147^{+13}_{-11}	60^{+33}_{-11}	5.6	$6.39^{+3.84}_{-2.67}$	3.5	$1.1^{+0.2}_{-0.1}$	$11.9^{+2.2}_{-1.4}$	$0.610^{0.109}_{0.068}$	$4.0^{0.6}_{0.4}$
HD131835†	9.430	1.899	83^{+0}_{-4}	87^{+4}_{-4}	6.2	$4.56^{+34.04}_{-2.71}$	$3.3^{+0.3}_{-0.9}$	$28.4^{+6.6}_{-6.0}$	$410.0^{+324.9}_{-509.3}$	$2.140^{0.499}_{0.452}$	$12.2^{2.8}_{2.6}$
HD76582	9.882	1.924	219^{+9}_{-20}	210^{+20}_{-20}	6.6	$5.92^{+17.58}_{-3.85}$	$3.6^{+0.3}_{-3.8}$	$2.4^{+1.5}_{-0.9}$	$18.1^{+35.0}_{-19.4}$	$2.442^{1.580}_{0.888}$	$12.7^{7.9}_{4.4}$
HD159492†	10.589	1.963	80^{+9}_{-21}	53^{+12}_{-22}	7.2	$13.22^{+2.74}_{-7.39}$	$4.8^{+1.0}_{-0.8}$	$0.4^{+0.1}_{-0.1}$	$0.1^{+3.2}_{-0.1}$	$0.036^{0.003}_{0.002}$	$0.8^{0.0}_{0.0}$
HD21997	10.850	1.976	94^{+3}_{-5}	52^{+5}_{-5}	7.5	$10.52^{+5.30}_{-3.80}$	$3.4^{+0.2}_{-0.2}$	$6.5^{+0.5}_{-0.5}$	$89.2^{+35.5}_{-35.6}$	$2.381^{0.186}_{0.196}$	$14.3^{1.1}_{1.2}$
HD20320	11.725	2.020	83^{+7}_{-23}	53^{+17}_{-23}	8.2	$15.85^{+43.96}_{-7.35}$	3.5	$0.2^{+0.0}_{-0.0}$	$2.3^{+0.4}_{-0.2}$	$0.288^{0.039}_{0.025}$	$2.8^{0.2}_{0.1}$
HD142091	12.014	2.035	102^{+4}_{-30}	66^{+21}_{-31}	8.5	$6.01^{+44.10}_{-5.83}$	$3.4^{+0.2}_{-5.83}$	$0.6^{+0.5}_{-14.5}$	$6.9^{+12.2}_{-14.5}$	$1.104^{0.820}_{0.150}$	$13.5^{5.0}_{0.9}$
HD131488†	12.162	2.042	92^{+1}_{-8}	46^{+7}_{-8}	8.6	$0.77^{+17.10}_{-0.66}$	$2.8^{+0.4}_{-0.5}$	$18.5^{+9.5}_{-7.4}$	$471.7^{+496.6}_{-308.0}$	$2.618^{1.350}_{1.047}$	$24.8^{12.8}_{9.9}$
HD153053	12.333	2.050	164^{+10}_{-65}	126^{+18}_{-66}	8.8	$5.34^{+36.18}_{-2.92}$	3.5	$0.8^{+0.3}_{-0.2}$	$8.6^{+3.6}_{-2.3}$	$0.680^{0.275}_{0.174}$	$3.9^{1.4}_{0.9}$
HD138965†	13.520	2.104	163^{+16}_{-3}	38^{+7}_{-3}	9.9	$4.71^{+0.37}_{-0.24}$	$3.7^{+0.1}_{-0.1}$	$5.2^{+0.2}_{-0.3}$	$57.1^{+1.9}_{-2.8}$	$1.663^{0.056}_{0.080}$	$8.4^{0.3}_{0.4}$
HD102647	13.695	2.112	31^{+2}_{-15}	24^{+5}_{-16}	10	$5.84^{+6.30}_{-2.93}$	$4.0^{+0.3}_{-0.9}$	$0.3^{+0.1}_{-0.1}$	$0.3^{+2.9}_{-4.7}$	$0.460^{0.058}_{0.035}$	$12.0^{0.2}_{0.1}$
HD121617	13.738	2.114	78^{+5}_{-10}	60^{+10}_{-10}	10	$1.68^{+0.34}_{-0.33}$	$3.5^{+0.1}_{-0.1}$	$55.4^{+4.8}_{-4.7}$	$661.4^{+165.7}_{-136.5}$	$2.208^{0.193}_{0.185}$	$12.7^{1.1}_{1.1}$
HD15257	14.455	2.145	270^{+60}_{-110}	220^{+100}_{-110}	11	$4.99^{+13.06}_{-2.94}$	$3.8^{+0.2}_{-1.2}$	$1.2^{+0.7}_{-0.2}$	$4.6^{+11.4}_{-25.0}$	$0.883^{0.495}_{0.174}$	$4.2^{1.8}_{0.6}$
HD183324†	14.659	2.154	130^{+20}_{-14}	34^{+49}_{-14}	11	$20.08^{+47.34}_{-14.21}$	3.5	$0.1^{+0.0}_{-0.0}$	$1.3^{+0.2}_{-0.1}$	$0.108^{0.013}_{0.011}$	$0.9^{0.1}_{0.1}$
HD70313	14.799	2.159	115^{+11}_{-14}	42^{+24}_{-14}	11	$5.35^{+38.70}_{-1.70}$	3.5	$1.0^{+0.2}_{-0.2}$	$10.4^{+2.1}_{-2.3}$	$0.479^{0.094}_{0.101}$	$2.9^{0.5}_{0.5}$
HD110411	14.951	2.166	94^{+6}_{-26}	56^{+24}_{-27}	11	$2.89^{+0.49}_{-1.00}$	$3.4^{+0.2}_{-0.2}$	$0.7^{+0.1}_{-0.0}$	$8.6^{+3.6}_{-2.8}$	$0.466^{0.035}_{0.025}$	$3.5^{0.2}_{0.1}$
HD9672†	15.020	2.169	136^{+2}_{-7}	147^{+8}_{-7}	11	$4.93^{+2.72}_{-1.21}$	$3.6^{+0.1}_{-0.2}$	$8.8^{+1.5}_{-1.4}$	$81.6^{+42.0}_{-38.2}$	$4.404^{0.729}_{0.698}$	$20.7^{3.4}_{3.2}$
HD12467	15.130	2.173	128^{+22}_{-22}	64^{+28}_{-23}	11	$14.21^{+53.53}_{-7.03}$	3.5	$1.3^{+0.1}_{-0.1}$	$14.0^{+1.2}_{-1.2}$	$0.703^{0.061}_{0.059}$	$4.3^{0.3}_{0.3}$
HD141378	15.375	2.183	126^{+10}_{-13}	60^{+19}_{-14}	12	$4.01^{+0.47}_{-0.28}$	3.5	$1.1^{+0.1}_{-0.1}$	$12.0^{+0.6}_{-0.8}$	$0.516^{0.025}_{0.032}$	$3.3^{0.1}_{0.2}$
HD31295†	15.555	2.190	105^{+5}_{-28}	64^{+21}_{-28}	12	$35.86^{+24.66}_{-27.19}$	$3.9^{+0.7}_{-1.2}$	$0.7^{+0.1}_{-0.1}$	$2.0^{+12.0}_{-17.2}$	$1.211^{0.127}_{0.092}$	$5.6^{0.5}_{0.3}$
HD216956	16.565	2.230	140^{+0}_{-0}	16^{+0}_{-0}	13	$8.29^{+4.64}_{-5.28}$	$3.5^{+0.1}_{-0.5}$	$0.8^{+0.2}_{-0.2}$	$8.2^{+5.2}_{-3.2}$	$27.697^{8.323}_{3.067}$	$163.6^{42.0}_{15.5}$
HD125162	17.339	2.259	81^{+6}_{-8}	18^{+2}_{-8}	14	$1.38^{+1.30}_{-1.17}$	$3.1^{+0.1}_{-0.1}$	$0.7^{+0.1}_{-0.1}$	$13.2^{+4.3}_{-3.6}$	$1.170^{0.162}_{0.146}$	$10.4^{1.2}_{1.1}$
HD17848	18.427	2.299	151^{+8}_{-41}	101^{+29}_{-41}	15	$25.52^{+48.42}_{-14.42}$	3.5	$0.5^{+0.6}_{-0.0}$	$5.5^{+0.6}_{-0.5}$	$0.979^{0.104}_{0.088}$	$5.9^{0.6}_{0.5}$
HD138813†	18.818	2.313	120^{+10}_{-20}	130^{+20}_{-20}	15	$9.64^{+3.47}_{-3.49}$	$3.3^{+0.1}_{-0.1}$	$5.9^{+0.6}_{-0.4}$	$89.2^{+22.3}_{-18.2}$	$1.256^{0.131}_{0.094}$	$8.2^{0.8}_{0.6}$
HD158352†	21.474	2.402	270^{+20}_{-60}	380^{+90}_{-60}	18	$0.99^{+9.86}_{-0.93}$	$3.3^{+0.2}_{-0.3}$	$1.0^{+0.6}_{-0.3}$	$16.5^{+14.9}_{-10.1}$	$2.207^{1.261}_{0.614}$	$17.2^{9.5}_{4.6}$
HD192425†	22.061	2.420	197^{+8}_{-40}	162^{+11}_{-40}	19	$24.81^{+34.61}_{-10.79}$	3.5	$0.4^{+0.0}_{-0.0}$	$4.2^{+0.5}_{-0.4}$	$1.420^{0.153}_{0.119}$	$8.5^{0.8}_{0.6}$
HD11413	22.674	2.439	175^{+23}_{-14}	41^{+28}_{-15}	19	$31.17^{+31.52}_{-13.53}$	3.5	$0.3^{+0.0}_{-0.0}$	$3.4^{+0.3}_{-0.2}$	$0.351^{0.026}_{0.024}$	$2.3^{0.1}_{0.1}$
HD54341	23.398	2.461	170^{+20}_{-50}	190^{+110}_{-50}	20	$5.26^{+21.09}_{-0.97}$	$3.6^{+0.2}_{-0.7}$	$3.5^{+0.4}_{-0.7}$	$27.1^{+18.7}_{-32.6}$	$0.762^{0.095}_{0.163}$	$3.4^{0.4}_{0.7}$
HD109573	23.899	2.476	77^{+0}_{0}	15^{+1}_{-1}	21	$2.45^{+0.40}_{-0.34}$	$3.5^{+0.1}_{-0.1}$	$58.3^{+4.8}_{-4.7}$	$611.3^{+136.8}_{-129.3}$	$5.744^{0.471}_{0.465}$	$26.9^{2.2}_{2.2}$
HD182681	26.538	2.552	143^{+4}_{-10}	100^{+10}_{-10}	24	$2.34^{+1.61}_{-2.01}$	$3.3^{+0.3}_{-0.2}$	$3.0^{+0.6}_{-0.8}$	$48.3^{+30.7}_{-20.7}$	$1.925^{0.411}_{0.510}$	$12.4^{2.6}_{3.2}$
HD38206†	27.005	2.564	180^{+20}_{-40}	120^{+30}_{-40}	24	$8.78^{+1.87}_{-2.15}$	$3.5^{+0.1}_{-0.1}$	$1.3^{+0.1}_{-0.1}$	$14.3^{+3.6}_{-3.6}$	$1.069^{0.047}_{0.044}$	$5.8^{0.2}_{0.2}$
HD14055	28.954	2.616	180^{+10}_{-20}	160^{+30}_{-20}	26	$2.64^{+0.53}_{-0.58}$	$3.4^{+0.1}_{-0.1}$	$1.0^{+0.1}_{-0.1}$	$12.2^{+2.7}_{-2.3}$	$2.657^{0.228}_{0.237}$	$16.2^{1.2}_{1.3}$
HD161868†	29.647	2.634	124^{+6}_{-10}	110^{+10}_{-10}	27	$14.25^{+13.75}_{-5.23}$	$3.6^{+0.2}_{-0.3}$	$0.7^{+0.1}_{-0.1}$	$6.3^{+3.7}_{-5.5}$	$2.186^{0.224}_{0.194}$	$13.1^{1.1}_{1.0}$
HD188228	32.152	2.695	130^{+10}_{-14}	38^{+25}_{-15}	30	$32.39^{+37.47}_{-18.68}$	3.5	$0.0^{+0.0}_{-0.0}$	$0.5^{+0.1}_{-0.1}$	$0.261^{0.031}_{0.024}$	$3.0^{0.2}_{0.1}$
HD142315	32.189	2.696	140	≤500	30	$1.34^{+0.42}_{-0.49}$	$4.0^{+0.2}_{-0.2}$	$7.9^{+1.1}_{-1.0}$	$2.6^{+37.4}_{-28.2}$	$0.177^{0.025}_{0.023}$	$0.7^{0.1}_{0.1}$
HD10939†	34.812	2.757	148^{+8}_{-21}	66^{+33}_{-21}	33	$20.53^{+16.55}_{-5.83}$	3.5	$1.0^{+0.1}_{-0.1}$	$11.0^{+0.9}_{-0.8}$	$1.376^{0.111}_{0.094}$	$7.8^{0.6}_{0.5}$
HD172167	55.933	3.157	118^{+4}_{-7}	67^{+9}_{-7}	61	$13.34^{+6.52}_{-7.17}$	$3.7^{+0.2}_{-0.2}$	$0.2^{+0.0}_{-0.0}$	$1.5^{+1.5}_{-1.2}$	$10.341^{1.667}_{0.792}$	$106.1^{6.8}_{3.2}$
HD13161	72.240	3.397	101^{+5}_{-41}	88^{+2}_{-41}	85	$10.66^{+4.41}_{-5.36}$	$3.3^{+0.2}_{-0.2}$	$0.5^{+0.1}_{-0.0}$	$6.5^{+2.7}_{-2.4}$	$1.358^{0.134}_{0.089}$	$13.2^{0.8}_{0.5}$
HD139006	72.664	3.403	41^{+4}_{-2}	14^{+2}_{-2}	86	$5.11^{+3.06}_{-2.17}$	3.5	$0.3^{+0.1}_{-0.0}$	$3.1^{+0.7}_{-0.5}$	$0.469^{0.053}_{0.038}$	$10.1^{0.2}_{0.2}$

This paper has been typeset from a TEX/LATEX file prepared by the author.